J. Fluid Mech. (2019), *vol.* 858, *pp.* 787–831. © Cambridge University Press 2018
doi:10.1017/jfm.2018.817

Effects of distributed roughness on crossflow instability through generalized resonance mechanisms

Jiyang He[1], Adam Butler[2] and Xuesong Wu[1,2,†]

[1]Laboratory of High-Speed Aerodynamics, School of Mechanical Engineering, Tianjin University, Tianjin 300072, PR China

[2]Department of Mathematics, Imperial College London, 180 Queen's Gate, London SW7 2AZ, UK

(Received 26 May 2018; revised 6 October 2018; accepted 6 October 2018; first published online 12 November 2018)

Experiments have shown that micron-sized distributed surface roughness can significantly promote transition in a three-dimensional boundary layer dominated by crossflow instability. This sensitive effect has not yet been fully explained physically and mathematically. Past studies focused on surface roughness exciting crossflow vortices and/or changing the local stability characteristics. The present paper seeks possible additional mechanisms by investigating the effects of distributed surface roughness on crossflow instability through resonant interactions with eigenmodes. A key observation is that the perturbation induced by roughness with specific wavenumbers can interact with two eigenmodes (travelling and stationary vortices) through triadic resonance, or interact with one eigenmode (stationary vortices) through Bragg scattering. Unlike the usual triadic resonance of neutral, or nearly neutral, eigenmodes, the present triadic resonance can take place among modes with $O(1)$ growth rates, provided that these are equal; unlike the usual Bragg scattering involving neutral waves, crossflow stationary vortices can also be unstable. For these amplifying waves, the generalized triadic resonance and Bragg scattering are put forward, and the resulting corrections to the growth rates are derived by a multiple-scale method. The analysis is extended to the case where up to four crossflow vortices interact with each other in the presence of suitable roughness components. The numerical results for Falkner–Skan–Cooke boundary layers show that roughness with a small height (a few percent of the local boundary-layer thickness) can change growth rates substantially (by a more-or-less $O(1)$ amount). This sensitive effect is attributed to two facts: (i) the resonant nature of the triadic interaction and Bragg scattering, which makes the correction to the growth rate proportional to the roughness height, and (ii) the wavenumbers of the roughness component required for the resonance are close to those of the neutral stationary crossflow modes, as a result of which a small roughness can generate a large response. Another important effect of roughness is that its presence renders the participating eigenmodes, which are otherwise independent, fully coupled. Our theoretical results suggest that micron-sized distributed surface roughness influences significantly both the amplification and spectral composition of crossflow vortices.

Key words: boundary layer stability, transition to turbulence, wave scattering

† Email address for correspondence: x.wu@ic.ac.uk

https://doi.org/10.1017/jfm.2018.817 Published online by Cambridge University Press

1. Introduction

It is known that laminar–turbulence transition in boundary layers is significantly influenced by surface roughness. The latter may be localized or distributed in one or both of the streamwise and spanwise directions. Depending on their forms, location, length scales and height, surface roughness elements may influence transition through different mechanisms, which include, as we shall discuss in more detail, receptivity, alteration of the baseflow thereby changing the instability characteristics and local scattering mechanism. Before proceeding to theoretical studies of the mechanisms, experimental observations about roughness are reviewed first.

For two-dimensional (2D) boundary layers, which are, in the absence of roughness, susceptible to the viscous Tollmien–Schlichting (T–S) instability, Klebanoff & Tidstrom (1972) observed that earlier transition was caused by an isolated 2D roughness with $h^*/\delta^* = 0.7 - 0.8$, where h^* is the roughness height and δ^* the boundary-layer displacement thickness. The flow is strongly destabilized in the separated region downstream of the roughness, where the inflectional profile is susceptible to a strong inviscid instability. Corke, Bar-Server & Morkovin (1986) studied the instability of 2D boundary layers with and without distributed roughness (sand paper) of the height $h^*/\delta^* \approx 0.5$. Although greatly enhanced growth of T–S waves was observed, the boundary-layer profile over a rough wall did not become inflectional, and kept a similar shape factor as that on the smooth wall. Therefore, the increased growth was not attributed to inviscid instability, but to the continual excitation of T–S waves on the rough wall by free-stream turbulence.

Mamun, Asai & Inasawa (2014) investigated the effects of sinusoidal surface corrugations with wavelengths of the same order of magnitude as that of the T–S waves in a zero-pressure-gradient boundary layer. The growth of the planar T–S mode was significantly enhanced by 2D corrugation even though its height $h^* = 0.1\delta^*$. In contrast, three-dimensional (3D) corrugations had only a small influence on the planar T–S wave even for a larger height $h^* = 0.2\delta^*$. On the other hand, 3D corrugations triggered, via interaction with the T–S modes, a pair of oblique waves, which amplify rapidly, causing the development of the Klebanoff-type peak–valley aligned structures. Hamed *et al.* (2016) carried out a laboratory investigation of transition over 2D and 3D periodic large-scale roughnesses. They found that the flow over the 2D roughness becomes turbulent much sooner than its 3D counterpart. This is likely due to the fact that flow separation (which leads to an inflectional profile) is less severe in the 3D case.

In 3D boundary layers, crossflow instability operates, leading to amplification of stationary and travelling vortices (Saric, Reed & White 2003). A series of wind-tunnel experiments on the effects of roughness on transition have been conducted since the 1990s. Reibert *et al.* (1996) and Carrillo, Reibert & Saric (1997) noted that naturally present surface irregularities with heights of microns (or submicron when polished) trigger stationary vortices, which grow to cause transition. Radeztsky, Reibert & Saric (1999) studied the impact of micron-sized distributed and isolated roughness elements in the boundary layer over a swept wing. For the case of the chordwise Reynolds number 2.7×10^6, as the surface was polished and background roughness height was reduced from 9.0 μm to 0.25 μm, the transition location was delayed from 40 % to 68 % of the chord length. This phenomenon indicates extreme sensitivity to micron-sized distributed roughness. They further pointed out that '[spanwise and chordwise] distributed roughness (random) appears to have the dangerous scales that effect transition'. On the other hand, when streamwise isolated and spanwise periodic roughness elements with 6 μm height were placed near the attachment line, earlier

https://doi.org/10.1017/jfm.2018.817 Published online by Cambridge University Press

transition was observed, which was attributed to stronger stationary vortices being excited by the roughness through receptivity. Carrillo *et al.* (1997) demonstrated experimentally that submicron-high discrete roughness elements (DREs), which are spanwise periodic and streamwise isolated, can influence transition significantly when applied near the attachment line. In particular, DREs with a spanwise spacing shorter than the wavelength of the linearly most unstable vortices delay transition. This surprising effect, together with the high sensitivity to roughness, led Saric, Carrillo & Reibert (1998) to suggest that DREs could be an effective laminar-flow-control technique. Its effectiveness has been assessed in a series of wind-tunnel and flight-test experiments (Carpenter, Saric & Reed 2008, 2009; Woodruff, Saric & Reed 2011). Woodruff *et al.* (2011) noted that the effectiveness of DREs is dependent on the free-stream turbulence level.

The theoretical approaches that account for surface roughness effects on boundary-layer transition can, according to the physical mechanisms being described, be divided into three categories: receptivity, instability and local scattering. Receptivity refers to the process in which external disturbances generate instability modes in the boundary layer (Goldstein & Hultgren 1989; Saric, Reed & Kerschen 2002). In order for roughness elements to excite instability modes, they must have a length scale comparable to the characteristic wavelength of the latter. If the modes to be excited are time-dependent (e.g. T–S waves/travelling vortices in 2D/3D boundary layers), the roughness-induced steady perturbation needs to interact with free-stream unsteady perturbations within a suitable frequency band, in order to produce the required forcing. In contrast, roughness in 3D boundary layers with suitable length scale can itself excite stationary crossflow vortices. Because the lower-branch neutral curve of crossflow eigenmodes is located near the leading edge, roughness in that region affects transition primarily through receptivity, and this receptivity is most effective and is considered to be the main factor contributing to the high sensitivity of transition. Crouch (1993) and Choudhari (1994) studied the receptivity of stationary modes to surface roughnesses using a finite-Reynolds-number theory (FRNT), which consists of the Orr–Sommerfeld (O–S) equation with the wall roughnesses being accounted for through inhomogeneous conditions. Using FRNT, Ng & Crouch (1999) calculated the initial amplitude pertaining to the experiment of Reibert *et al.* (1996), and the comparison with the measurements suggests that this FRNT works quite well. All of these studies neglected non-parallelism, which Bertolotti (2000) attempted to include by expanding the baseflow as a Taylor series. The FRNT based on the O–S equation is applicable only to roughness of sufficiently small height. Receptivity to large-height (nonlinear) roughness was considered by Choudhari & Duck (1996) using the high-Reynolds-number asymptotic approach.

Receptivity to surface roughness has also been studied by direct numerical simulations (DNS). Collis & Lele (1999) compared the predictions by DNS and FRNT, and found that neglecting non-parallel-flow effects led to over-prediction of the initial amplitudes, a conclusion that was later confirmed by Schrader, Brandt & Henningson (2009). Tempelmann *et al.* (2012) performed DNS of the receptivity process in the experiment of Reibert *et al.* (1996). The predicted amplitude is approximately 40 % of the measurement, and the discrepancy was attributed to an experimental uncertainty of the height and streamwise location of the roughness elements. Hosseini *et al.* (2013) investigated the receptivity to the DREs introduced for transition control, and their simulations confirmed the results of earlier experiments (Saric *et al.* 1998). The receptivity pertaining to the flight-test experiments (Carpenter *et al.* 2009) was modelled by Rizzetta *et al.* (2010) by DNS; however, no comparison was made

https://doi.org/10.1017/jfm.2018.817 Published online by Cambridge University Press

with experimental data. Kurz & Kloker (2014) simulated receptivity to micron-sized roughness elements, which were meshed, and found that the receptivity coefficient is not a constant as was often asserted, but a linear function of the roughness height. This behaviour, referred to as 'superlinearity', was shown theoretically to be an important feature of the receptivity near the leading edge (Butler & Wu 2018*a*).

Surface roughness, if present in the main unstable region, can influence transition by altering instability characteristics. Theoretical studies about this involve computing the roughness-modified mean flow and performing linear stability analysis of this new state. The effect of an isolated roughness (hump) in a 2D boundary layer was considered by Nayfeh, Ragab & Al-Maaitah (1988), Cebeci & Egan (1989), Masad & Iyer (1994) and Gao, Park & Park (2011). In order to capture possible flow separation created by the hump, the roughness-modified mean flow was computed by solving the interactive boundary-layer (IBL) equations or by DNS. Its linear stability was then studied based on the O–S equation or parabolized stability equations (PSE) (Gao *et al.* 2011; Park & Park 2013). Overall, the growth of T–S waves was enhanced. Clearly, for the PSE or the O–S equation to be applicable the streamwise length scale of the hump must be much longer than the characteristic T–S wavelength.

Similar studies have been carried out for distributed roughness (wavy walls). Lessen & Gangwani (1976) first calculated the response of a 2D boundary layer to small-amplitude surface waviness by solving the steady O–S equation subject to inhomogeneous boundary conditions. The resulting signature was used to evaluate the Reynolds stresses that modify the mean flow. The latter was obtained by solving the Reynolds-averaged boundary-layer equations. A linear stability analysis, based on the O–S equation for the modified mean flow, was performed. The effect is of $O(h^2)$, nevertheless, the calculation showed a 10 % reduction of the minimum critical Reynolds number in the presence of roughness with a height of only 1 % of the boundary-layer thickness. Gaster (2016) also computed the mean flow over a wavy wall using the O–S formulation. A linear stability analysis indicated increased amplification rates of T–S waves. Effects of wavy walls with a large enough amplitude to cause pockets of local separation were investigated by Wie & Malik (1998) and Thomas, Mughal & Ashworth (2017), who used respectively an IBL approach and a Navier–Stokes (N–S) solver to compute the roughness-modified mean flow. The development of T–S waves was then studied by the PSE approach. A wavy wall was found to play a destabilizing role in general. Thomas *et al.* (2017) found that shorter waviness has a stronger destabilizing effect, but some long-wavelength deformations create a favourable pressure gradient to damp the growth of T–S waves.

For 3D boundary layers, Masad (1996) considered streamwise localized and spanwise uniform surface waviness. The IBL approach was used to calculate the distorted mean flow, for which a linear stability analysis was performed. Thomas *et al.* (2016) considered extended chordwise surface waviness. The mean flow was computed by a N–S solver, and the stability of the distorted flow was assessed by PSE and linearized N–S methods. Both studies found that wavy walls enhanced the amplification of crossflow vortices. Note that the roughness heights considered by Thomas *et al.* (2016) were larger than 10 % of the displacement thickness, and their study is not pertinent to the experimental phenomenon for micron-sized distributed roughness.

Floryan (1997) investigated the effects of (simulated) wavy walls with short wavelengths comparable to the shear-layer thickness. Considering the spatial periodicity of the mean flow, Floquet theory was applied to study the stability. A new type of instability characterized by streamwise vortices as the dominant component

https://doi.org/10.1017/jfm.2018.817 Published online by Cambridge University Press

was found. The usual T–S waves were found to be moderately destabilized. Cabal, Szumbarski & Floryan (2002) used a similar methodology to study the stability of the flow in a wavy channel, and found two types of instability mode: streamwise vortices induced by the wall surface and T–S waves modified by the presence of wall waviness. The former might be caused by centrifugal effects over a wavy wall (Floryan 2002).

A different scenario occurs when a localized roughness is located in the main unstable region. An incoming instability wave will be scattered as it propagates through the streamwise inhomogeneous region created by the roughness. Of special interest is the roughness with length scale comparable to the characteristic wavelength of the instability, in which case neither the O–S equation nor PSE is valid due to the strong non-parallelism. Mathematically, this new mechanism of scattering is elliptic. A local scattering theory based on a triple-deck framework was proposed by Wu & Dong (2016). The impact of the localized roughness on transition was characterized naturally by a transmission coefficient, defined as the ratio of the amplitude of the T–S wave downstream of the roughness to that upstream. Their results showed that roughness played a destabilizing role. A finite-Reynolds-number formulation of the local scattering theory was developed by Huang & Wu (2017), and was verified by DNS results and experimental data, with which good agreement was obtained.

The mechanisms discussed above – receptivity, modification of instability and local scattering – all play an important role in influencing transition. In the present study, we seek possible additional ones which underpin the extreme sensitivity of crossflow instability and transition to micron-sized distributed roughness. Complementary to explanations based on those existing mechanisms, we try to understand the phenomenon from the perspective of resonant interactions between instability modes and the roughness-induced perturbation. Three-dimensional distributed roughness is modelled in the simplest case by a single Fourier component, or more realistically by a superposition of such components. The perturbation induced by each roughness component will be referred to as 'roughness mode' herein, despite the fact that it is not an eigenmode. We identify the components that can participate in some forms of resonant interactions with suitable crossflow eigenmodes, thereby changing the stability most effectively. Unlike previous stability analyses for the roughness-modified mean flow, which ignored wave–wave interaction, we retain the baseflow of a smooth wall, but let the disturbance be composed of roughness modes and crossflow eigenmodes. The resonant interactions can occur if their wavenumbers and frequencies satisfy certain resonance conditions, and these include triadic resonance between two crossflow eigenmodes and one roughness mode, and Bragg scattering involving one stationary crossflow eigenmode and one roughness mode. Triadic resonance is a general mechanism in wave mechanics, but was first proposed by Craik (1971) to describe the nonlinear evolution of T–S waves. It is usually required that the interacting waves have small growth rates, i.e. they are (nearly) neutral. The resonant triad in our study is a generalized one in that the crossflow eigenmodes involved can have $O(1)$ growth rates, and all that is needed is that their growth rates are (nearly) the same. Bragg scattering, which originated from crystallography, is a general wave phenomenon or mechanism as well. It was invoked, for example, to explain the strong reflection of water waves induced by periodic sandbars (Mei 1985; Mei, Hara & Naciri 1988), where the wavenumber and frequency of water waves are always real. Bragg scattering is generalized in our work to study the interaction of a roughness mode with an unstable crossflow eigenmode. Unlike local stability analysis, which requires the roughness wavelength to be much larger than that of instability modes,

https://doi.org/10.1017/jfm.2018.817 Published online by Cambridge University Press

the wavelengths of the roughness modes and crossflow eigenmodes in our resonant interactions can be comparable. Furthermore, the resonant interactions considered here involve multiple eigenmodes, whereas linear stability analysis involves only one eigenmode.

The rest of the paper is organized as follows. The problem is formulated in § 2, where after specifying the baseflow, we present the homogeneous and inhomogeneous boundary-value problems governing the crossflow eigenmodes and roughness modes respectively, and in particular the generalized resonance mechanisms are explained with reference to the dispersion relations of the crossflow vortices. The mathematical description of the resonant interactions is presented in § 3. Using a multiscale method, we derive the amplitude equations governing the interacting vortices; these equations allow us to compute the corrections to the growth rates. Numerical results are shown in § 4 for stationary and travelling crossflow vortices. Finally, the conclusions are summarized and topics of future investigations are discussed in § 5.

2. Problem formulation

2.1. *Governing equations*

We consider the three-dimensional incompressible boundary layer over a surface (of a swept wing or wedge), on which small-amplitude distributed surface roughness is present. The flow is described in the Cartesian coordinate system (x^*, y^*, z^*) with its origin at the leading edge, where x^*, y^* and z^* are in the chordwise, vertical and spanwise directions, respectively. The coordinates and velocities are non-dimensionalized by the local boundary-layer displacement thickness δ_0^* and chordwise slip velocity $U_{\infty,0}^*$ at the chordwise location x_0^* where the resonant interaction occurs, and x_0^* will be also referred to as the resonant point. The Reynolds number is defined as

$$Re = U_{\infty,0}^* \delta_0^* / \nu^*, \tag{2.1}$$

where ν^* is the kinematic viscosity.

The flow is governed by the non-dimensional incompressible N–S equations,

$$\frac{\partial \boldsymbol{u}}{\partial t} + (\boldsymbol{u}\cdot\boldsymbol{\nabla})\boldsymbol{u} + \boldsymbol{\nabla} p - \frac{1}{Re}\nabla^2 \boldsymbol{u} = 0, \quad \boldsymbol{\nabla}\cdot\boldsymbol{u} = 0, \tag{2.2}$$

where $\boldsymbol{u} = (u, v, w)$ with u, v and w standing for the chordwise, wall-normal and spanwise velocities respectively, and p denotes the pressure non-dimensionalized by $\rho^* U_{\infty,0}^{*2}$, with ρ^* being the reference density. The velocity and pressure, $(\boldsymbol{u}, p)$, are decomposed into a baseflow $(\boldsymbol{U}, P)$ and a disturbance part $(\boldsymbol{u}', p')$,

$$\boldsymbol{u} = \boldsymbol{U} + \boldsymbol{u}', \quad p = P + p'. \tag{2.3a,b}$$

The baseflow is assumed to be spanwise uniform. Its velocity field $\boldsymbol{U} = (U, V, W)$ satisfies the non-dimensional boundary-layer equations,

$$U\frac{\partial U}{\partial x} + V\frac{\partial U}{\partial y} = U_\infty \frac{\mathrm{d}U_\infty}{\mathrm{d}x} + \frac{1}{Re}\frac{\partial^2 U}{\partial y^2}, \tag{2.4a}$$

$$U\frac{\partial W}{\partial x} + V\frac{\partial W}{\partial y} = \frac{1}{Re}\frac{\partial^2 W}{\partial y^2}, \tag{2.4b}$$

$$\frac{\partial U}{\partial x} + \frac{\partial V}{\partial y} = 0, \tag{2.4c}$$

https://doi.org/10.1017/jfm.2018.817 Published online by Cambridge University Press

and the boundary conditions,

$$U = V = W = 0 \quad \text{at } y = 0; \quad U \to U_\infty, \quad W \to W_\infty \quad \text{as } y \to \infty, \tag{2.5a–c}$$

where U_∞ and W_∞ stand for the non-dimensional slip velocities along the chordwise and spanwise directions, respectively. Substituting the decomposition (2.3) into (2.2) and subtracting out the equations governing the baseflow lead to the nonlinear disturbance equations,

$$\frac{\partial \boldsymbol{u}}{\partial t} + (\boldsymbol{U}\cdot\boldsymbol{\nabla})\boldsymbol{u} + (\boldsymbol{u}\cdot\boldsymbol{\nabla})\boldsymbol{U} + \boldsymbol{\nabla} p - \frac{1}{Re}\nabla^2\boldsymbol{u} = -(\boldsymbol{u}\cdot\boldsymbol{\nabla})\boldsymbol{u}, \quad \boldsymbol{\nabla}\cdot\boldsymbol{u} = 0. \tag{2.6}$$

Without ambiguity, the prime symbol for disturbance quantities is omitted for simplicity.

2.2. *Baseflow*

The baseflow is taken to be the Falkner–Skan–Cooke (FSC) boundary layer, which has frequently been used as a convenient vehicle to investigate key receptivity, instability and transition mechanisms of three-dimensional boundary layers (e.g. Högberg & Henningson 1998; Schrader *et al.* 2009). The chordwise and spanwise slip velocities are given by

$$\frac{U^*_\infty(x^*)}{U^*_\infty(x^*_0)} = \left(\frac{x^*}{x^*_0}\right)^m, \quad W^*_\infty = \text{const.}, \tag{2.7a,b}$$

where the acceleration parameter m is related to the Hartree parameter β_H through the equation $m = \beta_H/(2-\beta_H)$. The local sweep angle ϕ_0 at the resonant point x^*_0 is defined as $\phi_0 = \tan^{-1}(W^*_\infty/U^*_\infty(x^*_0)) = \tan^{-1}(W_\infty)$ on noting that $U_\infty(x_0) = 1$. The values of m and ϕ_0 (or equivalently β_H and W_∞) can be chosen such that the profiles are representative of the local flow in the boundary layer over a swept wing.

This boundary-layer flow admits a similarity solution. Introducing a similarity variable η and a non-dimensional stream function Ψ,

$$\eta = \sqrt{\frac{m+1}{2}\frac{U_\infty Re}{x}}\,y, \quad \Psi = \sqrt{\frac{2}{m+1}\frac{U_\infty x}{Re}}\,f(\eta), \tag{2.8a,b}$$

we may express the baseflow velocities as $U = \partial\Psi/\partial y$, $V = -\partial\Psi/\partial x$ and $W = W_\infty g(\eta)$, substitution of which into (2.4) and (2.5) leads to the ordinary differential equations

$$f''' + ff'' + \beta_H(1 - f'^2) = 0, \quad g'' + fg' = 0, \tag{2.9a,b}$$

and the boundary conditions

$$f = f' = g = 0 \quad \text{at } \eta = 0; \quad f' = g' = 1 \quad \text{at } \eta = \infty, \tag{2.10a,b}$$

where the symbol $'$ stands for the derivative with respect to η.

By the standard definition, the boundary-layer displacement thickness is expressed as

$$\delta^*_0 = \left(\frac{m+1}{2}\frac{U^*_\infty(x^*_0)}{\nu^* x^*_0}\right)^{-1/2} c, \quad c = \int_0^\infty (1 - f')\,\mathrm{d}\eta. \tag{2.11}$$

https://doi.org/10.1017/jfm.2018.817 Published online by Cambridge University Press

Non-dimensionalizing the first of the above equations gives the relation between the non-dimensional resonant point x_0 and the corresponding Reynolds number Re, $x_0 = (m+1)Re/(2c^2)$ (Högberg & Henningson 1998).

The dimensionless velocities within the boundary layer and their derivatives (with respect to y) can be expressed as

$$U(y) = f'(\eta), \quad \frac{\mathrm{d}U}{\mathrm{d}y} = cf''(\eta); \quad W(y) = W_\infty g(\eta), \quad \frac{\mathrm{d}W}{\mathrm{d}y} = W_\infty c g'(\eta). \tag{2.12a–d}$$

2.3. *Crossflow eigenmodes*

According to usual linear stability theory, crossflow eigenmodes, which may be present in the absence of roughness, take the normal-mode form,

$$(u, v, w, p) = \epsilon(\hat{u}, \hat{v}, \hat{w}, \hat{p})E + \text{c.c.}, \quad E = \mathrm{e}^{\mathrm{i}(\alpha x + \beta z - \omega t)}, \tag{2.13}$$

where α and β are the chordwise and spanwise wavenumbers, respectively, ω is the frequency and $\epsilon \ll 1$ is a measure of the amplitude. If the Reynolds number Re is taken to be asymptotically large, a variety of long-wavelength regimes (with $\alpha, \beta \ll 1$) arises (Choudhari 1995). In the present work, we treat Re as being finite, but make the usual parallel-flow approximation, with which substitution of (2.13) into (2.6) leads to a system of the first-order equations,

$$\frac{\mathrm{d}\hat{\boldsymbol{\varphi}}}{\mathrm{d}y} = \boldsymbol{L}\hat{\boldsymbol{\varphi}}, \tag{2.14}$$

where the vector $\hat{\boldsymbol{\varphi}} = [\hat{u}, \hat{v}, \hat{w}, D\hat{u}, \hat{p}, D\hat{w}]^{\mathrm{T}}$, and the operator $\boldsymbol{L}$ is given by

$$\boldsymbol{L} = \begin{bmatrix} 0 & 0 & 0 & 1 & 0 & 0 \\ -\mathrm{i}\alpha & 0 & -\mathrm{i}\beta & 0 & 0 & 0 \\ 0 & 0 & 0 & 0 & 0 & 1 \\ ReS & ReDU & 0 & 0 & \mathrm{i}\alpha Re & 0 \\ 0 & -S & 0 & -\mathrm{i}\alpha/Re & 0 & -\mathrm{i}\beta/Re \\ 0 & ReDW & ReS & 0 & \mathrm{i}\beta Re & 0 \end{bmatrix}, \tag{2.15}$$

with $S = -\mathrm{i}\omega + \mathrm{i}\alpha U + \mathrm{i}\beta W + (\alpha^2 + \beta^2)/Re$ and D standing for $\mathrm{d}/\mathrm{d}y$. The boundary conditions follow from the requirements that the perturbation velocities vanish at the smooth wall and decay to zero in the free stream, and so they can be expressed as

$$\hat{u}(y) = \hat{v}(y) = \hat{w}(y) = 0 \quad \text{at } y = 0; \quad \hat{u}(y), \hat{v}(y), \hat{w}(y) \to 0 \quad \text{as } y \to \infty. \tag{2.16a,b}$$

By eliminating $\hat{p}$, $\hat{u}$ and $\hat{w}$, the system (2.14) can be reduced to the well-known O–S equation for $\hat{v}$,

$$\left[(-\mathrm{i}\omega + \mathrm{i}\alpha U + \mathrm{i}\beta W)(D^2 - \alpha^2 - \beta^2) - \mathrm{i}\alpha U'' - \mathrm{i}\beta W'' - \frac{1}{Re}(D^2 - \alpha^2 - \beta^2)^2\right]\hat{v} = 0, \tag{2.17}$$

but we will solve the eigenvalue problem (2.14)–(2.16) in the primitive variables, for which an efficient algorithm exists (Malik 1990). The present finite-Reynolds-number formulation represents a composite theory valid for all long-wavelength (and possibly

https://doi.org/10.1017/jfm.2018.817 Published online by Cambridge University Press

viscous) regimes (Choudhari 1995) except the lower-branch regime, where non-parallelism is a leading-order effect (Butler & Wu 2018*a*). We are concerned with spatial stability, and so the chordwise wavenumber α is calculated for a given spanwise wavenumber β and frequency ω. Usually $\alpha = \alpha_r + \mathrm{i}\alpha_i$ is complex, with $-\alpha_i$ representing the growth rate. The instability modes are referred to as travelling vortices if $\omega \neq 0$ and stationary vortices if $\omega = 0$.

The eigenvalue problem posed by (2.14) and the boundary conditions (2.16) is solved numerically. The equation is discretized by using the fourth-order compact finite-difference scheme of Malik (1990). The resulting algebraic system has non-zero solutions only when the determinant of its coefficient matrix is equal to zero. For a given α, β and ω, the determinant is computed by Gaussian elimination, and an appropriate α making the determinant vanish is found by Müller iteration.

2.4. *Roughness modes*

In general, the wall shape can be represented as a superposition of Fourier components,

$$y_w = \sum_{\alpha_w, \beta_w} h(\alpha_w, \beta_w) \mathrm{e}^{\mathrm{i}(\alpha_w x + \beta_w z)} + \text{c.c.}, \tag{2.18}$$

where α_w and β_w are the chordwise and spanwise roughness wavenumbers, respectively. As the roughness height h^* of interest is approximately several microns, which amounts to a few percent of the boundary-layer thickness δ_0^*, it is appropriate to assume that the non-dimensional height $h \equiv h^*/\delta_0^*$ is small enough that a perturbative mathematical scheme is deemed applicable. Then each Fourier mode is independent, and we can calculate the boundary-layer response to each Fourier component,

$$y_w = h\mathrm{e}^{\mathrm{i}(\alpha_w x + \beta_w z)} + \text{c.c.}, \tag{2.19}$$

which is to be referred to as single-wavenumber roughness, and a more general form (2.18) will be referred to as a multiple-wavenumber roughness. Random background roughness consists of a wide range of spatial wavelengths, possibly from several microns to millimetres. We will in the present paper identify more dangerous components that affect crossflow vortices more effectively than others do. It turned out that those components have length scales comparable to wavelengths of crossflow instability, which are in millimetres in laboratory conditions.

Under the local parallel-flow assumption, the perturbation induced by (2.19) takes the form,

$$[u_w, v_w, w_w, p_w] = h[\hat{u}_w(y), \hat{v}_w(y), \hat{w}_w(y), \hat{p}_w(y)]\mathrm{e}^{\mathrm{i}(\alpha_w x + \beta_w z)} + \text{c.c.}, \tag{2.20}$$

where $\hat{u}_w(y)$ and etc. are shape functions. Introducing (2.20) into (2.6) leads to the O–S equation for $\hat{v}_w$,

$$\left[(\mathrm{i}\alpha_w U + \mathrm{i}\beta_w W)(D^2 - \alpha_w^2 - \beta_w^2) - \mathrm{i}\alpha_w U'' - \mathrm{i}\beta_w W'' - \frac{1}{Re}(D^2 - \alpha_w^2 - \beta_w^2)^2\right]\hat{v}_w = 0, \tag{2.21}$$

or equivalently the first-order system,

$$\frac{\mathrm{d}\hat{\boldsymbol{\varphi}}_w}{\mathrm{d}y} = \boldsymbol{L}_w\hat{\boldsymbol{\varphi}}_w, \tag{2.22}$$

https://doi.org/10.1017/jfm.2018.817 Published online by Cambridge University Press

where $\hat{\boldsymbol{\varphi}}_w$ and $\boldsymbol{L}_w$ have similar expressions as $\hat{\boldsymbol{\varphi}}$ and $\boldsymbol{L}$ in (2.14)–(2.15) for crossflow eigenmodes. At the wavy wall, the no-slip condition must be satisfied. By performing Taylor expansion about $y = 0$ for $h \ll 1$ and using the fact that $U_B(0) = W_B(0) = V_B'(0) = 0$ for a viscous boundary-layer flow, the boundary is shifted to $y = 0$, leading to the inhomogeneous boundary conditions (cf. Choudhari 1994),

$$\hat{u}_w(0) = -U'(0), \quad \hat{v}_w(0) = 0, \quad \hat{w}_w(0) = -W'(0). \tag{2.23a–c}$$

The boundary conditions in the far field are

$$\hat{u}_w(y), \hat{v}_w(y), \hat{w}_w(y) \to 0 \quad \text{as } y \to \infty. \tag{2.24}$$

The assumption underlying linearization and the simplified boundary condition (2.23) is now made more precise and further justified. With $h \ll 1$, the induced motion is primarily within a viscous sublayer layer with an $O(R\mathrm{e}^{-1/3}\delta_0^*)$ thickness near the wall, where the perturbation is $O(h)$ (Choudhari & Duck 1996). The perturbation in the sublayer is linear if $h \ll R\mathrm{e}^{-1/3}$, but becomes nonlinear when $h = O(R\mathrm{e}^{-1/3})$. For both linear and nonlinear regimes, the sublayer is governed by the steady boundary-layer equations, the Prandtl transform can be applied to convert the boundary to $y = 0$ while keeping the equations exactly invariant, and the induced motion in the main layer is $O(R\mathrm{e}^{-1/3}h)$ and remains linear. For the three-dimensional layers of interest, typically $Re = O(10^3)$, and so nonlinearity within the sublayer is expected when $h = O(10^{-1})$. Our focus here is, however, on $h = O(10^{-2})$, and so it is reasonable to assume that $h \ll R\mathrm{e}^{-1/3}$, for which the roughness mode is linear in the entire boundary layer.

Discretization of (2.22) and its boundary conditions (2.23), (2.24) by the fourth-order compact finite-difference scheme leads to an inhomogeneous system of linear algebraic equations, which is solved for given roughness wavenumbers β_w and α_w to obtain the shape functions of the roughness mode.

2.5. *Generalized resonance mechanisms*

When crossflow eigenmodes and roughness mode are present simultaneously in the boundary layer, interactions between them take place. Of particular interest are interactions of resonant nature, occurring at the quadratic order. These include triadic resonance and Bragg scattering generalized to unstable eigenmodes. Consider two crossflow eigenmodes with carrier waves $E_1 = \mathrm{e}^{\mathrm{i}(\alpha_1 x + \beta_1 z - \omega_1 t)}$ and $E_2 = \mathrm{e}^{\mathrm{i}(\alpha_2 x + \beta_2 z - \omega_2 t)}$, and one roughness mode $E_w = \mathrm{e}^{\mathrm{i}(\alpha_w x + \beta_w z)}$. One of the eigenmodes interacts with the roughness mode to generate the other and vice versa, and this may take place in the two forms:

$$E_1 = E_2 E_w, \tag{2.25}$$

and

$$E_1 = E_2^* E_w, \tag{2.26}$$

where the superscript $*$ denotes the complex conjugate. For (2.25) and (2.26) to hold, the corresponding wavenumbers and frequencies must satisfy the resonance conditions

$$\left.\begin{array}{ll} \mathrm{Im}\,\alpha_1 = \mathrm{Im}\,\alpha_2, & \omega_1 = \omega_2, \\ \mathrm{Re}\,\alpha_1 - \mathrm{Re}\,\alpha_2 = \alpha_w, & \beta_1 - \beta_2 = \beta_w, \end{array}\right\} \tag{2.27}$$

and

$$\left.\begin{array}{ll} \mathrm{Im}\,\alpha_1 = \mathrm{Im}\,\alpha_2, & \omega_1 = -\omega_2, \\ \mathrm{Re}\,\alpha_1 + \mathrm{Re}\,\alpha_2 = \alpha_w, & \beta_1 + \beta_2 = \beta_w, \end{array}\right\} \tag{2.28}$$

https://doi.org/10.1017/jfm.2018.817 Published online by Cambridge University Press

respectively. These two forms of resonance will be referred to as triad difference and triad sum, respectively. Each set of the resonance conditions has two parts: the first specifies the requirements that must be satisfied by the eigenmodes involved in the resonance, and the second determines the wavenumbers of the participating roughness mode. For the triad difference, the growth rates and frequencies of the two eigenmodes must be equal, and the roughness wavenumbers are the differences of those of the two eigenmodes; for the triad sum, the growth rates must also be equal but the frequencies must be of opposite sign, and the roughness wavenumbers are the sums of those of the two eigenmodes. That these conditions can be satisfied will be illustrated below with reference to the dispersion characteristics of crossflow vortices.

There is a special case for the triad sum where the two eigenmodes are identical. The corresponding resonance conditions become

$$\left.\begin{array}{c} \omega = 0, \\ 2\mathrm{Re}\,\alpha = \alpha_w, \quad 2\beta = \beta_w. \end{array}\right\} \tag{2.29}$$

This kind of resonance will be referred to as generalized Bragg scattering, which can take place between any stationary eigenmode and the roughness element with wavenumbers twice those of the former.

The triad difference, triad sum and Bragg scattering are referred to as the generalized resonance mechanisms in this paper. A roughness component satisfying one of the resonant conditions (2.27)–(2.29) is of special significance as it produces, through quadrati interactions, an $O(h)$ correction to the growth rates of crossflow vortices. In contrast, non-resonant components influence each eigenmode via interactions at cubic order as follows. At the quadratic level, the roughness mode interacts with itself to generate an $O(h^2)$ mean-flow distortion, and it also interact with the eigenmode to produce an $O(\epsilon h)$ forcing on the Fourier components $(\alpha_1 \pm \alpha_w, \beta_1 \pm \beta_w)$, which are not eigenmodes as none of (2.27)–(2.29) are satisfied, and the responses are thus finite. At the cubic order, the mean-flow distortion and $(\alpha_1 \pm \alpha_w, \beta_1 \pm \beta_w)$ interact with the eigenmode and the roughness mode, respectively, both reproducing the eigenmode whose magnitude is $O(h^2\epsilon)$. The resulting effect is a much smaller $O(h^2)$ correction to the growth rate.

The crossflow eigenmodes and roughness modes satisfying the resonance conditions of the generalized resonance mechanisms are searched for stationary and non-stationary cases by applying the first part of each set of the resonance conditions. This requires computation of unstable crossflow eigenmodes by linear stability analysis. For illustration, the results for the baseflow parameters of $\phi_0 = 45^\circ$, $m = 0.34207$, $Re = 338$ and 2000 are presented here; the value of m is taken to be the same as in Högberg & Henningson (1998) so that our linear stability results can be validated by comparison with theirs. Figure 1 displays the results for the stationary case. As figure 1(*a*) shows, the variation of α_r against β is almost linear, which is a remarkable property and will have an important implication for resonance. Figure 1(*b*) shows that instability exists $(-\alpha_i > 0)$ in an interval of β, the ends of which correspond to two neutral eigenmodes, both of which turn out to be relevant for understanding the response of the boundary layer to roughness. Unstable modes to the left/right of the most unstable one will be referred to as left/right branches, respectively. The schematic of resonance for stationary vortices is shown in figure 1(*b*). Two stationary vortices can have equal growth rate $(-\alpha_i)$, and they are denoted as E1 and E2 in the figure. They can interact with each other in the presence of suitable roughness through the triad difference and triad sum, referred to as $1-2$ and $1+2$,

https://doi.org/10.1017/jfm.2018.817 Published online by Cambridge University Press

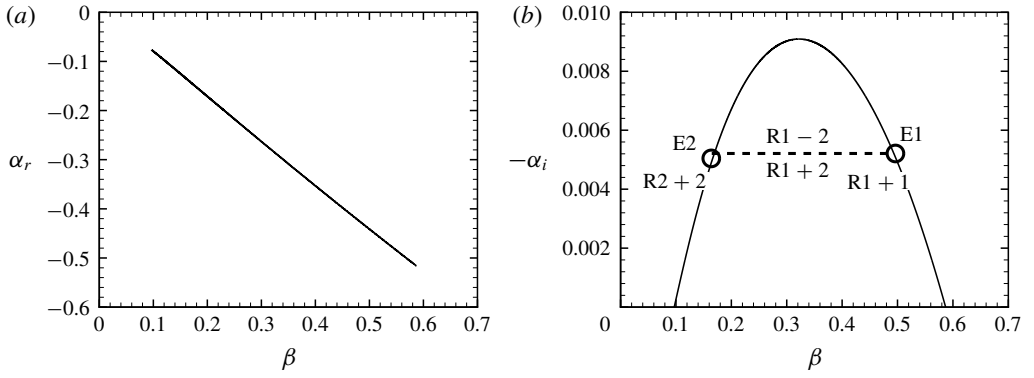


FIGURE 1. Instability characteristics of stationary vortices for the parameters: $\phi_0 = 45°$, $m = 0.34207$ and $Re = 338$. (*a*) The variation of α_r with β. (*b*) The variation of $-\alpha_i$ with β and the schematic of the resonances, where the letters 'E' and 'R' stand for eigenmode and roughness mode, respectively. The eigenmodes with the same growth rate are designated by numbers 1 and 2, and the $\pm$ signs signify the triadic difference/sum interactions.

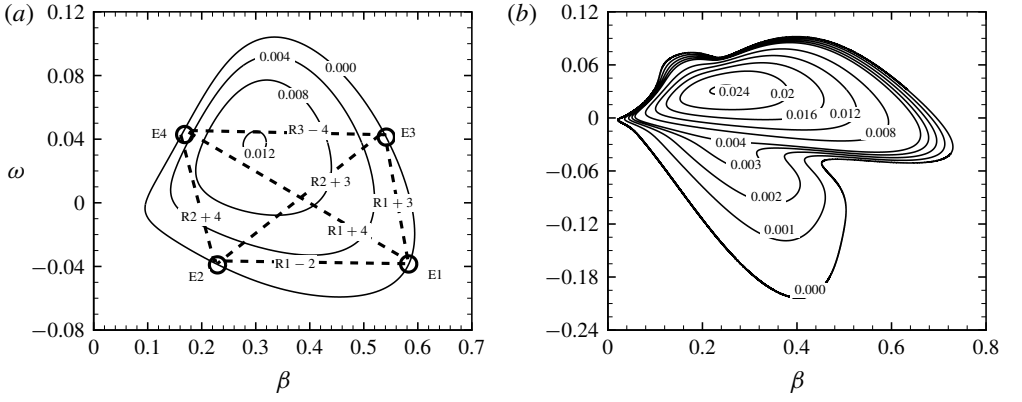


FIGURE 2. Contours of growth rate and schematic of the resonances for travelling vortices. The parameters are $\phi_0 = 45°$, $m = 0.34207$, (*a*) $Re = 338$ and (*b*) $Re = 2000$. The letters 'E' and 'R' stand for 'eigenmode' and 'roughness mode', respectively.

respectively. Furthermore, each mode may interact with a roughness mode through Bragg scattering, denoted by $1 + 1$ and $2 + 2$, respectively. Note that the crossflow eigenmodes are denoted by numbers, and the roughness modes are designated by numbers and symbols '+' and '−', indicating that the resonance mechanism involved is the triad sum and difference, respectively. Stationary eigenmodes 1 and 2 can also interact with a multiple-wavenumber roughness comprised of the four components, in which case multiple generalized resonance mechanisms take effect at the same time.

Now we turn to resonances involving travelling vortices. Figure 2 shows the contours of the growth rate at a low and a high Reynolds number. For the former, every contour line is convex so that we can locate up to four travelling eigenmodes with equal $|\omega|$ and $-\alpha_i$, which are labelled as E1, E2, E3 and E4 in figure 2(*a*). The frequency of travelling vortices 1 and 2 is negative, and that of 3 and 4 is positive.

https://doi.org/10.1017/jfm.2018.817 Published online by Cambridge University Press

These four travelling vortices can interact with six single-wavenumber components, which are $1+3$, $1+4$, $2+3$ and $2+4$ through the triad sum, and $1-2$ and $3-4$ through the triad difference. Figure 2(*b*) indicates that at a higher Re contour lines of small growth rates can be concave for certain range of β and ω, where up to six travelling eigenmodes with equal $|\omega|$ and $-\alpha_i$ may be located. For simplicity, in this paper we concentrate only on the case of four travelling eigenmodes, but the methodology can be easily extended to the more complex case.

There exist connections between stationary and non-stationary cases. When the frequency of the four travelling eigenmodes is reduced to zero, eigenmodes 3 and 4 coalesce with 1 and 2, respectively. It follows that roughness $3-4$ becomes the same as $1-2$, while roughnesses $1+4$ and $2+3$ collapse, both becoming equivalent to roughness $1+2$ for the stationary case; see figure 1(*b*). Roughnesses $1+3$ and $2+4$ become $1+1$ and $2+2$, respectively, i.e. these triad-sum interactions degenerate into Bragg scattering.

3. Mathematical description of resonant interactions between crossflow eigenmodes and roughness modes

In the presence of distributed surface roughness (waviness), the evolution and even the composition of the crossflow eigenmodes will be different from the flat-surface case, due to the resonant interactions with the roughness modes at the quadratic order. In order to quantify the effects of distributed roughness, the interactions must be analysed. A large-Reynolds-number asymptotic analysis is performed by Butler & Wu (2018*b*) for stationary vortices. In the present study, we will take a finite-Reynolds-number approach, and consider both travelling and stationary vortices. Using a multiscale method, we will derive the amplitude equations for the eigenmodes, first for their interactions with a single-wavenumber roughness. The analysis will then be extended to the case of multiple-wavenumber roughness. The quadratic interactions cause an $O(h)$ correction to the growth rate. In order to account for this effect, we introduce a slow variable $\bar{x} = hx$, and let the amplitudes of the eigenmodes be functions of this slow variable.

3.1. *Interaction of eigenmodes with single-wavenumber roughness: triad difference*

The interaction through the triad difference (2.27) involves two eigenmodes j and k, and one single-wavenumber roughness. The disturbance ϕ (standing for u, v, w and p), comprising of the roughness mode and the eigenmodes, can be represented by

$$\phi = h[\hat{\phi}_w E_w + \text{c.c.}] + \epsilon[A_j(\bar{x})\hat{\phi}_{j0}(y)E_j + h\hat{\phi}_{j1}E_j + \text{c.c.}] + \epsilon[A_k(\bar{x})\hat{\phi}_{k0}(y)E_k + h\hat{\phi}_{k1}E_k + \text{c.c.}], \tag{3.1}$$

where $E_w = \mathrm{e}^{\mathrm{i}(\alpha_w x+\beta_w z)}$, $E_j = \mathrm{e}^{\mathrm{i}(\alpha_j x+\beta_j z-\omega_j t)}$ and $E_k = \mathrm{e}^{\mathrm{i}(\alpha_k x+\beta_k z-\omega_k t)}$. A_j and A_k denote the amplitude functions of the respective eigenmodes. Substituting (3.1) into (2.6), at $O(\epsilon)$ and $O(h)$ we recover respectively the eigenvalue problem and the inhomogeneous problem determining the roughness mode. At $O(\epsilon h)$, we obtain the equations for $\hat{\phi}_{j1}$ and $\hat{\phi}_{k1}$,

$$\frac{\mathrm{d}\hat{\boldsymbol{\varphi}}_{j1}}{\mathrm{d}y} = \boldsymbol{L}_j\hat{\boldsymbol{\varphi}}_{j1} + \frac{\mathrm{d}A_j}{\mathrm{d}\bar{x}}\boldsymbol{f}_j + A_k\boldsymbol{f}_{k-w}, \tag{3.2a}$$

$$\frac{\mathrm{d}\hat{\boldsymbol{\varphi}}_{k1}}{\mathrm{d}y} = \boldsymbol{L}_k\hat{\boldsymbol{\varphi}}_{k1} + \frac{\mathrm{d}A_k}{\mathrm{d}\bar{x}}\boldsymbol{f}_k + A_j\boldsymbol{f}_{j-w^*}, \tag{3.2b}$$

https://doi.org/10.1017/jfm.2018.817 Published online by Cambridge University Press

where $\hat{\boldsymbol{\varphi}}_{j,k1}$ and $\boldsymbol{L}_{j,k}$ have the same relations to the dependent variables and linear operators as $\hat{\boldsymbol{\varphi}}$ and $\boldsymbol{L}$ in (2.14)–(2.15) provided that α and β are replaced by $\alpha_{j,k}$ and $\beta_{j,k}$ respectively. The inhomogeneous terms are

$$\left.\begin{aligned}\boldsymbol{f}_j &= [0,\, -f_j^c,\, 0,\, Ref_j^x,\, -Df_j^c/Re - f_j^y,\, Ref_j^z]^{\mathrm{T}},\\ \boldsymbol{f}_{k-w} &= [0,\, 0,\, 0,\, Ref_{k-w}^x,\, -f_{k-w}^y,\, Ref_{k-w}^z]^{\mathrm{T}},\end{aligned}\right\} \tag{3.3}$$

where

$$f_j^x = \left(U - \frac{2\mathrm{i}\alpha_j}{Re}\right)\hat{u}_{j0} + \hat{p}_{j0}, \quad f_j^y = \left(U - \frac{2\mathrm{i}\alpha_j}{Re}\right)\hat{v}_{j0}, \quad f_j^z = \left(U - \frac{2\mathrm{i}\alpha_j}{Re}\right)\hat{w}_{j0}, \quad f_j^c = \hat{u}_{j0}, \tag{3.4a–d}$$

and the Reynolds stresses

$$f_{k-w}^x = \mathrm{i}\alpha_w\hat{u}_{k0}\hat{u}_w + \mathrm{i}\alpha_k\hat{u}_{k0}\hat{u}_w + \hat{v}_{k0}D\hat{u}_w + D\hat{u}_{k0}\hat{v}_w + \mathrm{i}\beta_w\hat{w}_{k0}\hat{u}_w + \mathrm{i}\beta_k\hat{u}_{k0}\hat{w}_w, \tag{3.5}$$

$$f_{k-w}^y = \mathrm{i}\alpha_w\hat{u}_{k0}\hat{v}_w + \mathrm{i}\alpha_k\hat{v}_{k0}\hat{u}_w + \hat{v}_{k0}D\hat{v}_w + D\hat{v}_{k0}\hat{v}_w + \mathrm{i}\beta_w\hat{w}_{k0}\hat{v}_w + \mathrm{i}\beta_k\hat{v}_{k0}\hat{w}_w, \tag{3.6}$$

$$f_{k-w}^z = \mathrm{i}\alpha_w\hat{u}_{k0}\hat{w}_w + \mathrm{i}\alpha_k\hat{w}_{k0}\hat{u}_w + \hat{v}_{k0}D\hat{w}_w + D\hat{w}_{k0}\hat{v}_w + \mathrm{i}\beta_w\hat{w}_{k0}\hat{w}_w + \mathrm{i}\beta_k\hat{w}_{k0}\hat{w}_w. \tag{3.7}$$

The expression for $\boldsymbol{f}_k$ follows from $\boldsymbol{f}_j$ by changing j to k, and the expression for $\boldsymbol{f}_{j-w^*}$ from $\boldsymbol{f}_{k-w}$ by the substitutions: $k \to j$, $(\alpha_w,\, \beta_w) \to (-\alpha_w,\, -\beta_w)$ and $\phi_w \to \phi_w^*$. The corresponding boundary conditions at $y = 0$ for (3.2) are given by

$$\hat{u}_{j1}(0) = -A_k\hat{u}'_{k0}(0), \quad \hat{v}_{j1}(0) = 0, \quad \hat{w}_{j1}(0) = -A_k\hat{w}'_{k0}(0); \tag{3.8a}$$

$$\hat{u}_{k1}(0) = -A_j\hat{u}'_{j0}(0), \quad \hat{v}_{k1}(0) = 0, \quad \hat{w}_{k1}(0) = -A_j\hat{w}'_{j0}(0). \tag{3.8b}$$

The far-field boundary conditions are homogeneous as usual.

In order for the inhomogeneous boundary-value problem (3.2*a*) with (3.8*a*), or (3.2*b*) with (3.8*b*), to have a solution, a solvability condition must be satisfied. This can be derived by reducing (3.2*a*) or (3.2*b*) to an inhomogeneous O–S equation, and then using the adjoint eigenfunction. Alternatively, we may discretize (3.2*a*) and (3.2*b*), and apply Gaussian elimination to the resulting algebraic systems. Either way, we obtain two coupled amplitude equations,

$$\frac{\mathrm{d}A_j}{\mathrm{d}\bar{x}} + F_{k-w}A_k(\bar{x}) = 0, \tag{3.9a}$$

$$\frac{\mathrm{d}A_k}{\mathrm{d}\bar{x}} + F_{j-w^*}A_j(\bar{x}) = 0, \tag{3.9b}$$

where F_{k-w} and F_{j-w^*} are constants calculated by applying the solvability condition; the two procedures mentioned above give the same value for each of these constants.

The amplitude equations (3.9) can be rearranged into the matrix form

$$\frac{\mathrm{d}}{\mathrm{d}\bar{x}}[A_j,\, A_k]^{\mathrm{T}} = \boldsymbol{F}[A_j,\, A_k]^{\mathrm{T}}, \tag{3.10}$$

with $\boldsymbol{F}$ being the 2×2 matrix,

$$\boldsymbol{F} = -\begin{bmatrix} 0 & F_{k-w} \\ F_{j-w^*} & 0 \end{bmatrix}. \tag{3.11}$$

https://doi.org/10.1017/jfm.2018.817 Published online by Cambridge University Press

Seeking solutions of the exponential form,

$$[A_j, A_k]^{\mathrm{T}} = \boldsymbol{a}\mathrm{e}^{\lambda\bar{x}} = [a_j, a_k]^{\mathrm{T}}\mathrm{e}^{\lambda\bar{x}}, \tag{3.12}$$

leads to an eigenvalue problem

$$\lambda\boldsymbol{a} = \boldsymbol{F}\boldsymbol{a}. \tag{3.13}$$

The physical meanings of the eigenvalue $\lambda = \lambda_r + \mathrm{i}\lambda_i$ and eigenvector $\boldsymbol{a}$ are now analysed. In terms of $\boldsymbol{a}$ and λ, the chordwise disturbance velocity u_j and u_k at the leading order can be written as

$$A_j\hat{u}_{j0}E_j = a_j\hat{u}_{j0}\mathrm{e}^{(\lambda_r h - \mathrm{Im}\,\alpha_j)x}\mathrm{e}^{\mathrm{i}(\mathrm{Re}\,\alpha_j x + \lambda_i h x + \beta_j z - \omega_j t)}, \tag{3.14a}$$

$$A_k\hat{u}_{k0}E_k = a_k\hat{u}_{k0}\mathrm{e}^{(\lambda_r h - \mathrm{Im}\,\alpha_k)x}\mathrm{e}^{\mathrm{i}(\mathrm{Re}\,\alpha_k x + \lambda_i h x + \beta_k z - \omega_k t)}, \tag{3.14b}$$

indicating that the new growth rates are $(\lambda_r h - \mathrm{Im}\,\alpha_j)$ for eigenmode j and $(\lambda_r h - \mathrm{Im}\,\alpha_k)$ for eigenmode k after the resonant interaction. The growth rates of both eigenmodes j and k are modified by $\lambda_r h$, which is proportional to the roughness height h. We define the scaling factor as the growth-rate correction coefficient, which is dependent only on the resonant triad. The latter is uniquely determined by a pair of $(-\alpha_i, \omega)$, and the growth-rate correction coefficient λ_r is therefore a function of $-\alpha_i$ and ω,

$$\lambda_r = \lambda_r(-\alpha_i, \omega). \tag{3.15}$$

The eigenvector $\boldsymbol{a}$ represents the ratio of the amplitudes of the two interacting eigenmodes. The amplitude ratio, defined as

$$\rho(-\alpha_i, \omega) = |a_j/a_k|, \tag{3.16}$$

is also a function of $-\alpha_i$ and ω. It transpires that the two eigenmodes are coupled by small-amplitude roughness, whereas they are independent of each other for the smooth-wall case in the linear regime.

3.2. *Interaction of eigenmodes with single-wavenumber roughness: triad sum*

The disturbance ϕ remains of the form (3.1). By a similar procedure as that for the triad difference (2.28), the equations at $O(\epsilon h)$ are given as

$$\frac{\mathrm{d}\hat{\boldsymbol{\varphi}}_{j1}}{\mathrm{d}y} = \boldsymbol{L}_{j0}\hat{\boldsymbol{\varphi}}_{j1} + \frac{\mathrm{d}A_j}{\mathrm{d}\bar{x}}\boldsymbol{f}_j + A_k^*\boldsymbol{f}_{k^*-w}, \tag{3.17a}$$

$$\frac{\mathrm{d}\hat{\boldsymbol{\varphi}}_{k1}}{\mathrm{d}y} = \boldsymbol{L}_{k0}\hat{\boldsymbol{\varphi}}_{k1} + \frac{\mathrm{d}A_k}{\mathrm{d}\bar{x}}\boldsymbol{f}_k + A_j^*\boldsymbol{f}_{j^*-w}, \tag{3.17b}$$

where $\boldsymbol{f}_j$ and $\boldsymbol{f}_k$ have the same expressions as those for the triad difference, and $\boldsymbol{f}_{k^*-w}$ is given by

$$\boldsymbol{f}_{k^*-w} = [0, 0, 0, Ref^x_{k^*-w}, -f^y_{k^*-w}, Ref^z_{k^*-w}]^{\mathrm{T}}, \tag{3.18}$$

with the Reynolds stresses

$$f^x_{k^*-w} = \mathrm{i}\alpha_w\hat{u}^*_{k0}\hat{u}_w - \mathrm{i}\alpha^*_k\hat{u}^*_{k0}\hat{u}_w + \hat{v}^*_{k0}D\hat{u}_w + D\hat{u}^*_{k0}\hat{v}_w + \mathrm{i}\beta_w\hat{w}^*_{k0}\hat{u}_w - \mathrm{i}\beta_k\hat{u}^*_{k0}\hat{w}_w, \tag{3.19}$$

$$f^y_{k^*-w} = \mathrm{i}\alpha_w\hat{u}^*_{k0}\hat{v}_w - \mathrm{i}\alpha^*_k\hat{v}^*_{k0}\hat{u}_w + \hat{v}^*_{k0}D\hat{v}_w + D\hat{v}^*_{k0}\hat{v}_w + \mathrm{i}\beta_w\hat{w}^*_{k0}\hat{v}_w - \mathrm{i}\beta_k\hat{v}^*_{k0}\hat{w}_w, \tag{3.20}$$

$$f^z_{k^*-w} = \mathrm{i}\alpha_w\hat{u}^*_{k0}\hat{w}_w - \mathrm{i}\alpha^*_k\hat{w}^*_{k0}\hat{u}_w + \hat{v}^*_{k0}D\hat{w}_w + D\hat{w}^*_{k0}\hat{v}_w + \mathrm{i}\beta_w\hat{w}^*_{k0}\hat{w}_w - \mathrm{i}\beta_k\hat{w}^*_{k0}\hat{w}_w. \tag{3.21}$$

https://doi.org/10.1017/jfm.2018.817 Published online by Cambridge University Press

The expression for $\boldsymbol{f}_{j^*-w}$ follows from $\boldsymbol{f}_{k^*-w}$ by replacing k by j. The corresponding boundary conditions at $y=0$ are

$$\hat{u}_{j1} = -A_k^*\hat{u}_{k0}^{*'}(0), \quad \hat{v}_{j1}=0, \quad \hat{w}_{j1}=-A_k^*\hat{w}_{k0}^{*'}(0); \tag{3.22a}$$

$$\hat{u}_{k1} = -A_j^*\hat{u}_{j0}^{*'}(0), \quad \hat{v}_{k1}=0, \quad \hat{w}_{k1}=-A_j^*\hat{w}_{j0}^{*'}(0), \tag{3.22b}$$

and the boundary conditions far away from the wall are homogeneous as usual.

Applying solvability conditions to (3.17*a*) with (3.22*a*) and (3.17*b*) with (3.22*b*) leads to two coupled amplitude equations

$$\frac{\mathrm{d}A_j}{\mathrm{d}\bar{x}} + F_{k^*-w}A_k^* = 0, \tag{3.23a}$$

$$\frac{\mathrm{d}A_k}{\mathrm{d}\bar{x}} + F_{j^*-w}A_j^* = 0. \tag{3.23b}$$

Note that the above two complex equations are somewhat different from (3.9*a*)–(3.9*b*) in that they involve complex conjugates of the amplitude functions. Decoupling them into four real equations, we can recast the system into the matrix form,

$$\frac{\mathrm{d}}{\mathrm{d}\bar{x}}[\mathrm{Re}\,A_j, \mathrm{Im}\,A_j, \mathrm{Re}\,A_k, \mathrm{Im}\,A_k]^{\mathrm{T}} = \boldsymbol{F}[\mathrm{Re}\,A_j, \mathrm{Im}\,A_j, \mathrm{Re}\,A_k, \mathrm{Im}\,A_k]^{\mathrm{T}}, \tag{3.24}$$

where the 4×4 coefficient matrix

$$\boldsymbol{F} = -\begin{bmatrix} 0 & 0 & \mathrm{Re}\,F_{k^*-w} & \mathrm{Im}\,F_{k^*-w} \\ 0 & 0 & \mathrm{Im}\,F_{k^*-w} & -\mathrm{Re}\,F_{k^*-w} \\ \mathrm{Re}\,F_{j^*-w} & \mathrm{Im}\,F_{j^*-w} & 0 & 0 \\ \mathrm{Im}\,F_{j^*-w} & -\mathrm{Re}\,F_{j^*-w} & 0 & 0 \end{bmatrix} \tag{3.25}$$

is real-valued. Equation (3.24) admits solutions of the exponential form,

$$[\mathrm{Re}\,A_j, \mathrm{Im}\,A_j, \mathrm{Re}\,A_k, \mathrm{Im}\,A_k]^{\mathrm{T}} = \tfrac{1}{2}(\boldsymbol{a}\mathrm{e}^{\lambda\bar{x}} + \mathrm{c.c.}), \tag{3.26}$$

substituting of which into (3.24) yields the eigenvalue problem, $\lambda\boldsymbol{a} = \boldsymbol{F}\boldsymbol{a}$. The real part of λ, λ_r, represents the growth-rate correction coefficient, the same as that for the triad difference. However, the definition of the amplitude ratio ρ for the triad sum is different. Note that the eigenvector $\boldsymbol{a}$ can be expressed in the polar form,

$$\boldsymbol{a} = [a_{j1}, a_{j2}, a_{k1}, a_{k2}]^{\mathrm{T}} = [|a_{j1}|\mathrm{e}^{\mathrm{i}\theta_{j1}}, |a_{j2}|\mathrm{e}^{\mathrm{i}\theta_{j2}}, |a_{k1}|\mathrm{e}^{\mathrm{i}\theta_{k1}}, |a_{k2}|\mathrm{e}^{\mathrm{i}\theta_{k2}}]^{\mathrm{T}}. \tag{3.27}$$

According to (3.24), (3.26) and (3.27), the modulus of $A_{j,k}$ can be expressed as

$$|A_{j,k}|^2 = \mathrm{e}^{2\lambda_r\bar{x}}|a_{j,k}|^2 = \mathrm{e}^{2\lambda_r\bar{x}}[|a_{j,k1}|^2\cos^2(\lambda_i\bar{x}+\theta_{j,k1}) + |a_{j,k2}|^2\cos^2(\lambda_i\bar{x}+\theta_{j,k2})]. \tag{3.28}$$

For the triad sum, with the coefficient matrix $\boldsymbol{F}$ given by (3.25), the elements of the eigenvector $\boldsymbol{a}$ satisfy

$$a_{j1} = \mathrm{i}a_{j2}, \quad a_{k1} = \mathrm{i}a_{k2}, \tag{3.29a,b}$$

from which it follows $|a_{j1}| = |a_{j2}|$, $|a_{k1}| = |a_{k2}|$, $\theta_{j1} = \theta_{j2} + \pi/2$ and $\theta_{k1} = \theta_{k2} + \pi/2$. The amplitude ratio ρ for the triad sum is thus defined as

$$\rho(-\alpha_i, \omega) = |a_{j1}|/|a_{k1}|. \tag{3.30}$$

https://doi.org/10.1017/jfm.2018.817 Published online by Cambridge University Press

For the interaction between the eigenmodes and multiple-wavenumber roughness, which will be discussed later, the relations in (3.29) may not hold. Using trigonometric identities, $a_{j,k}$ can be expressed as

$$|a_{j,k}|^2 = G_{j,k}\cos(2\lambda_i\bar{x}) - H_{j,k}\sin(2\lambda_i\bar{x}) + (|a_{j,k1}|^2 + |a_{j,k2}|^2)/2, \tag{3.31}$$

where $G_{j,k} = |a_{j,k1}|^2\cos(2\theta_{j,k1})/2 + |a_{j,k2}|^2\cos(2\theta_{j,k2})/2$ and $H_{j,k} = |a_{j,k1}|^2\sin(2\theta_{j,k1})/2 + |a_{j,k2}|^2\sin(2\theta_{j,k2})/2$. The maximum value of $|a_{j,k}|$ is given by

$$|a_{j,k}|^2_{max} = \sqrt{G^2_{j,k} + H^2_{j,k}} + (|a_{j,k1}|^2 + |a_{j,k2}|^2)/2. \tag{3.32}$$

Now the amplitude ratio is defined as

$$\rho = |a_j|_{max}/|a_k|_{max}, \tag{3.33}$$

from which we can recover (3.30) with $|a_{j,k}|_{max} = |a_{j,k1}|$ following from the relations in (3.29). Note that for the triad sum the frequencies of the two eigenmodes are of opposite sign. We use the positive one as the control parameter for λ_r and ρ.

For stationary vortices, the triad difference and sum both operate, but an additional interaction, Bragg scattering, exists. Following a similar procedure as for the triad sum, the amplitude equation can be derived as

$$\frac{\mathrm{d}A}{\mathrm{d}\bar{x}} + F_w A^* = 0, \tag{3.34}$$

which can be rewritten into a 2×2 system for $[\mathrm{Re}\,A,\ \mathrm{Im}\,A]^{\mathrm{T}}$. The growth-rate correction coefficient for Bragg scattering can be obtained by the same method as that for the triad sum. Since only one stationary eigenmode is involved in Bragg scattering, the issue of amplitude ratio does not arise.

3.3. *Interaction of crossflow eigenmodes with multiple-wavenumber roughness*

The analysis is now extended to the interactions between crossflow eigenmodes and multiple-wavenumber roughness. Stationary and non-stationary cases must be considered separately due to different forms of resonance.

Two stationary vortices with the same growth rate can in general interact simultaneously with four roughness modes: namely, the triad sum and difference interactions with $(\alpha_{w_{1\pm2}}, \beta_{w_{1\pm2}})$, and Bragg scattering by $(\alpha_{w_{1+1}}, \beta_{w_{1+1}})$ and $(\alpha_{w_{2+2}}, \beta_{w_{2+2}})$. The disturbance comprised of these modes takes the form,

$$\begin{aligned}\phi \;=\; & h(\hat{\phi}_{w_{1-2}}E_{w_{1-2}} + \text{c.c.}) + h(\hat{\phi}_{w_{1+2}}E_{w_{1+2}} + \text{c.c.}) \\ & + h(\hat{\phi}_{w_{1+1}}E_{w_{1+1}} + \text{c.c.}) + h(\hat{\phi}_{w_{2+2}}E_{w_{2+2}} + \text{c.c.}) \\ & + \epsilon[A_1(\bar{x})\hat{\phi}_{10}(y)E_1 + h\hat{\phi}_{11}E_1 + \text{c.c.}] + \epsilon[A_2(\bar{x})\hat{\phi}_{20}(y)E_2 + h\hat{\phi}_{21}E_2 + \text{c.c.}].\end{aligned} \tag{3.35}$$

Following similar steps as before, we can derive the two coupled amplitude equations,

$$\frac{\mathrm{d}A_1}{\mathrm{d}\bar{x}} + \mathcal{F}_{2-w_{1-2}}A_2(\bar{x}) + \mathcal{F}_{2^*-w_{1+2}}A_2^*(\bar{x}) + \mathcal{F}_{1^*-w_{1+1}}A_1^*(\bar{x}) \;=\; 0, \tag{3.36a}$$

$$\frac{\mathrm{d}A_2}{\mathrm{d}\bar{x}} + \mathcal{F}_{1-w^*_{1-2}}A_1(\bar{x}) + \mathcal{F}_{1^*-w_{1+2}}A_1^*(\bar{x}) + \mathcal{F}_{2^*-w_{2+2}}A_2^*(\bar{x}) \;=\; 0. \tag{3.36b}$$

https://doi.org/10.1017/jfm.2018.817 Published online by Cambridge University Press

The above two complex equations are again recast into a system of four real equations akin to (3.24). Seeking exponential solutions to the system, we obtain an eigenvalue problem, $\lambda \boldsymbol{a} = \boldsymbol{F}\boldsymbol{a}$, with $\boldsymbol{F}$ being a 4×4 real-valued matrix.

For travelling vortices, resonances can take place among four travelling eigenmodes (with equal α_i and $|\omega|$) and six roughness modes. The disturbance consisting of these components takes the form,

$$\begin{aligned}\phi \;=\; & h(\hat{\phi}_{w_{1-2}} E_{w_{1-2}} + \text{c.c.}) + h(\hat{\phi}_{w_{1+3}} E_{w_{1+3}} + \text{c.c.}) + h(\hat{\phi}_{w_{1+4}} E_{w_{1+4}} + \text{c.c.}) \\ & + h(\hat{\phi}_{w_{2+3}} E_{w_{2+3}} + \text{c.c.}) + h(\hat{\phi}_{w_{2+4}} E_{w_{2+4}} + \text{c.c.}) + h(\hat{\phi}_{w_{3-4}} E_{w_{3-4}} + \text{c.c.}) \\ & + \epsilon[A_1(\bar{x})\hat{\phi}_{10}(y)E_1 + h\hat{\phi}_{11}E_1 + \text{c.c.}] + \epsilon[A_2(\bar{x})\hat{\phi}_{20}(y)E_2 + h\hat{\phi}_{21}E_2 + \text{c.c.}] \\ & + \epsilon[A_3(\bar{x})\hat{\phi}_{30}(y)E_3 + h\hat{\phi}_{31}E_3 + \text{c.c.}] + \epsilon[A_4(\bar{x})\hat{\phi}_{40}(y)E_4 + h\hat{\phi}_{41}E_4 + \text{c.c.}]. \quad (3.37)\end{aligned}$$

Following similar steps as before, we can derive the four coupled amplitude equations,

$$\frac{\mathrm{d}A_1}{\mathrm{d}\bar{x}} + F_{2-w_{1-2}}A_2 + F_{3^*-w_{1+3}}A_3^* + F_{4^*-w_{1+4}}A_4^* = 0, \quad (3.38a)$$

$$\frac{\mathrm{d}A_2}{\mathrm{d}\bar{x}} + F_{1-w_{1-2}^*}A_1 + F_{3^*-w_{2+3}}A_3^* + F_{4^*-w_{2+4}}A_4^* = 0, \quad (3.38b)$$

$$\frac{\mathrm{d}A_3}{\mathrm{d}\bar{x}} + F_{1^*-w_{1+3}}A_1^* + F_{2^*-w_{2+3}}A_2^* + F_{4-w_{3-4}}A_4 = 0, \quad (3.38c)$$

$$\frac{\mathrm{d}A_4}{\mathrm{d}\bar{x}} + F_{1^*-w_{1+4}}A_1^* + F_{2^*-w_{2+4}}A_2^* + F_{3-w_{3-4}^*}A_3 = 0. \quad (3.38d)$$

The above four complex equations need to be decomposed into a system of eight real equations. Seeking exponential solutions leads to an eigenvalue problem, $\lambda \boldsymbol{a} = \boldsymbol{F}\boldsymbol{a}$, with $\boldsymbol{F}$ being a 8×8 real-valued matrix.

For multiple-wavenumber cases, the growth-rate correction coefficient λ_r can be defined as the largest real part of the eigenvalues, and the amplitude ratio ρ is computed by a procedure described earlier; see (3.31)–(3.33).

The mathematical description of the resonant interactions assumes that the surface roughness is comprised of one or several Fourier components that have suitable wavenumbers to facilitate the resonances between the crossflow vortices. However, given the fact that it is not uncommon that instability modes satisfying resonant conditions develop out of broadband and even random background disturbances (Medeiros & Gaster 1999; Borodulin, Kachanov & Koptsev 2002), we think that the restriction to such spatially quasiperiodic patterned roughness may be unnecessary. The mechanisms could operate even if such patterns are submerged in the background surface roughness consisting of a broad range of scales, because the crossflow vortices having the same growth rate could select the required components from all those that are present.

4. Numerical results

We now compute the growth-rate correction coefficient and amplitude ratio for representative baseflow parameters. The acceleration parameter m is set to be 0.34207, 0.5 and 1.0. A local sweep angle of 45° and two different Reynolds numbers (338 and 2000) are chosen.

https://doi.org/10.1017/jfm.2018.817 Published online by Cambridge University Press

4.1. *Resonant interactions of stationary vortices with roughness modes*

Before presenting the growth-rate correction coefficients and amplitude ratios, a parametric study is performed to monitor the eigenmodes and roughness modes including their wavenumbers and shape functions, as the information is helpful for understanding the sensitive role of roughness. For brevity, the results are presented for $m = 0.5$; our calculations indicate that those for other values of m are similar.

In order to describe the high-Reynolds-number characteristics of eigenmodes and roughness modes, the concept of a critical level for the stationary crossflow eigenmode and roughness mode is introduced. For the former, the O–S equation (2.17) in the high-Reynolds-number limit reduces to the Rayleigh equation

$$(D^2 - \alpha^2 - \beta^2)\hat{v} = \frac{\alpha U'' + \beta W''}{\alpha U + \beta W}\hat{v}. \tag{4.1}$$

The singularity of this equation occurs at the critical level y_c, which coincides with an inflection point, and thus

$$\alpha U(y_c) + \beta W(y_c) = 0, \quad \alpha U''(y_c) + \beta W''(y_c) = 0. \tag{4.2a,b}$$

By eliminating the wavenumbers, we obtain the equation

$$U(y_c)/U''(y_c) = W(y_c)/W''(y_c), \tag{4.3}$$

which allows us to compute y_c from the baseflow before solving the eigenvalue problem. In the case of $\phi_0 = 45^\circ$ and $m = 0.5$, it is found that $y_c = 1.9915$.

A roughness mode satisfies the forced Rayleigh equation in the inviscid limit, and it also has a critical level y_{cw}, which is given by

$$\alpha_w U(y_{cw}) + \beta_w W(y_{cw}) = 0. \tag{4.4}$$

In figure 3, the roughness wavenumbers (β_w, α_w) satisfying the resonance conditions of the triad sum, triad difference and Bragg scattering for stationary vortices are compared with (β_s^r, α_s^r), where β_s^r and α_s^r are the spanwise and chordwise wavenumbers of the right-branch neutral stationary eigenmode, respectively. We note that (β_w, α_w) in the triad sum are close to (β_s^r, α_s^r) for all growth rates; this closeness occurs also in Bragg scattering around the largest growth rate, and in the triad difference near the smallest growth rate $(-\alpha_i = 0)$. These features of roughness wavenumbers come from the linear instability characteristics of stationary vortices shown in figure 1(*a*): the wavenumbers of the left-branch neutral eigenmode are much smaller than those of the right-branch neutral eigenmode, and α_r varies with β almost linearly. Therefore, the sum and difference of their wavenumbers are close to (β_s^r, α_s^r) when $\alpha_i = 0$. The sum of the spanwise wavenumbers of unstable eigenmodes 1 and 2 with equal growth rate turns out to be β_s^r approximately, i.e. $\beta_1 + \beta_2 \approx \beta_s^r$, for all $-\alpha_i$. The linear relation implies that the second resonant condition, $\alpha_1 + \alpha_2 = \alpha_s^r$, is automatically satisfied. Since the triad sum degenerates to Bragg scattering at the largest growth rate, where eigenmodes 1 and 2 are identical, the roughness wavenumbers in Bragg scattering around the largest growth rate are close to (β_s^r, α_s^r). As the growth rate decreases, the roughness wavenumbers in Bragg scattering deviate from (β_s^r, α_s^r), whereas the opposite is true for the triad difference. With the Reynolds number increased, the roughness wavenumbers in the triad sum become closer to (β_s^r, α_s^r) generally, as indicated by figure 3(*b*,*d*).

https://doi.org/10.1017/jfm.2018.817 Published online by Cambridge University Press

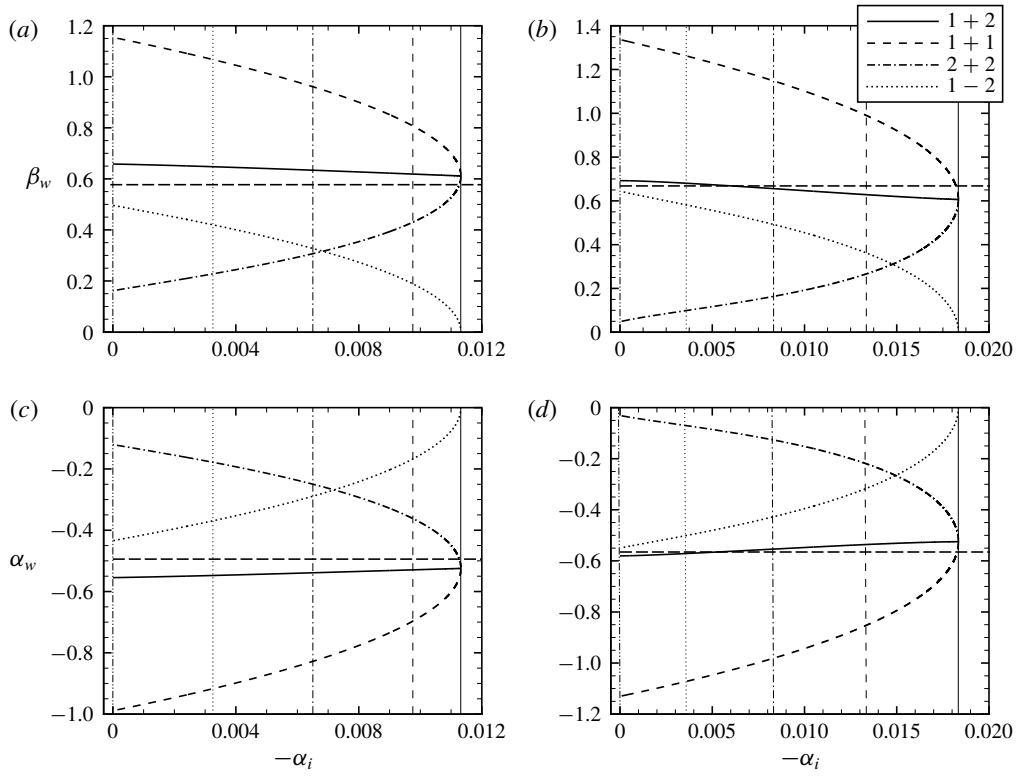


FIGURE 3. Variations of the roughness wavenumbers satisfying the resonance conditions of the triad sum $(1+2)$, triad difference $(1-2)$ and Bragg scattering $(1+1$ and $2+2)$ with the growth rate for stationary vortices at $m=0.5$. The long dashed lines stand for β_s^r and α_s^r, the wavenumbers of the right-branch neutral stationary eigenmodes. (*a*,*c*) $Re=338$; (*b*,*d*) $Re=2000$.

In Bragg scattering, there is the relation $(\beta_w, \alpha_w) = (2\beta, 2\alpha_r(\beta))$. On the other hand, the crossflow eigenmode $(\beta, \alpha(\beta))$ generates the harmonic $(2\alpha, 2\alpha(\beta))$. Since α_i is numerically small, the harmonic and the roughness mode are likely to be fairly close to each other. Furthermore, the nearly linear relation between α_r and β implies that $\alpha_r(2\beta) \approx 2\alpha_r(\beta)$. It follows that the roughness mode is probably also close to the eigenmode $(2\beta, \alpha(2\beta))$ if $\beta \leqslant \beta_s^r/2$.

The shape functions of the stationary vortices and roughness modes in a resonant triad are monitored for the five cases marked by the thin vertical lines in figure 3. The growth rates and wavenumbers of these eigenmodes are listed in table 1. Among these cases, the stationary vortices are nearly most unstable in case 1 and neutral in case 5. The exactly most unstable stationary eigenmode is not chosen because the corresponding difference of its wavenumbers is zero, in which case the equations governing the roughness-induced perturbation degenerate (and non-parallelism needs to be accounted for in order to resolve this degeneracy). The eigenfunctions of the eigenmodes 1 located on the right branch are shown in figure 4(*a*,*b*) for $Re = 338$ and 2000. Note that eigenfunctions are normalized by the maximum value of $|\hat{u}|$. For brevity, only the chordwise disturbance velocity $|\hat{u}|$ is displayed since the spanwise disturbance velocity $|\hat{w}|$ closely resembles $|\hat{u}|$. At $Re = 338$, the vertical position

https://doi.org/10.1017/jfm.2018.817 Published online by Cambridge University Press

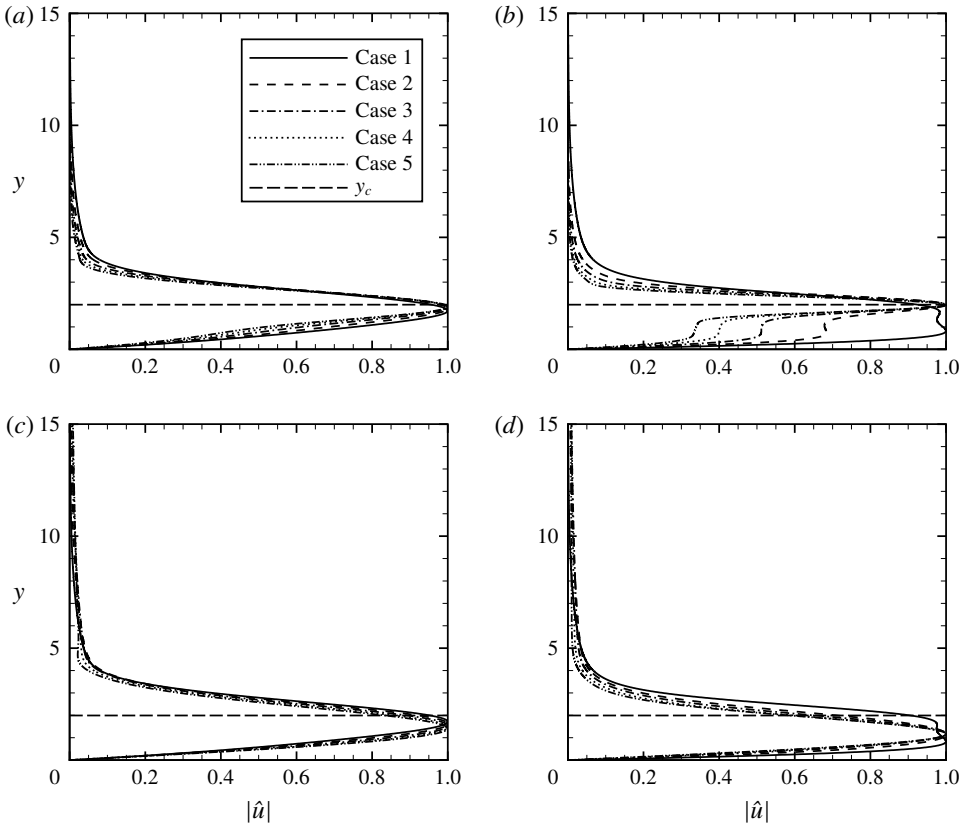


FIGURE 4. The eigenfunctions of the eigenmodes on the right branch (*a*,*b*) and left branch (*c*,*d*): (*a*,*c*) $Re = 338$; (*b*,*d*) $Re = 2000$.

y_m of the maximum value of the eigenfunction for the neutral eigenmode of case 5 is closest to the critical level y_c among all cases. Although the eigenmodes of cases 1–4 are unstable, their y_m are also fairly close to y_c. As the Reynolds number increases, the eigenfunctions in cases 2–5 feature a two-layer structure. Inspecting, for example, the eigenfunctions at $Re = 2000$ of eigenmodes with low growth rates, one observes a wall layer, where viscosity cannot be ignored. Towards the outer edge of the wall layer, the eigenfunctions tend to constants. The perturbation concentrates in the so-called critical layer surrounding y_c. The positions of the maxima of the eigenfunctions are extremely close to y_c. For the nearly most unstable eigenmode in case 1, the wall layer and the critical layer are not distinct, which is expected since the critical-layer concept is not attainable. The above observations suggest that right-branch stationary eigenmodes are essentially inviscid. The critical-layer concept, which originates from inviscid instability for neutral stationary modes, is applicable to right-branch unstable stationary eigenmodes provided that their growth rates are not too large, and the Reynolds number is high enough. The eigenfunctions of the eigenmodes 2 located on the left branch for the five cases are shown in figure 4(*c*,*d*). They do not exhibit a two-layer structure as right-branch eigenmodes do. Nevertheless, the positions of their maxima are fairly close to y_c as well.

The shape functions of the roughness modes for the chosen cases are now presented. Figure 5 shows the results for the roughness modes interacting with stationary

https://doi.org/10.1017/jfm.2018.817 Published online by Cambridge University Press

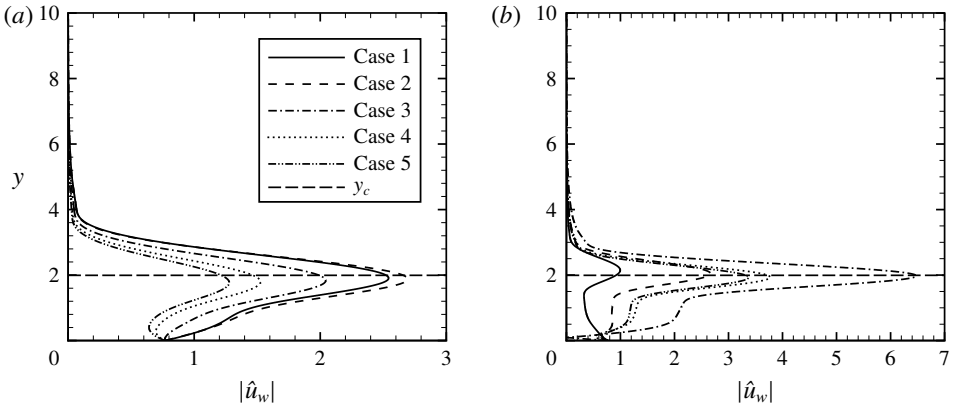


FIGURE 5. Distribution of the roughness modes in the triad sum (1 + 2) interaction: (*a*) $Re = 338$; (*b*) $Re = 2000$.

	α_i	β_1	$\mathrm{Re}\,\alpha_1$	β_2	$\mathrm{Re}\,\alpha_2$
		(*a*) $Re = 338$			
Case 1	−0.0113134	0.3113300	−0.2673790	0.2999562	−0.2572778
Case 2	−0.0097570	0.4037300	−0.3482950	0.2150391	−0.1809680
Case 3	−0.0065036	0.4805300	−0.4139413	0.1533736	−0.1248766
Case 4	−0.0032529	0.5337300	−0.4585129	0.1138362	−0.0891467
Case 5	0.0000000	0.5772319	−0.4943765	0.0809225	−0.0603090
		(*b*) $Re = 2000$			
Case 1	−0.0183378	0.3091000	−0.2676515	0.2971172	−0.2571380
Case 2	−0.0133520	0.4951000	−0.4260816	0.1332301	−0.1099216
Case 3	−0.0083213	0.5741000	−0.4905781	0.0818596	−0.0633355
Case 4	−0.0035869	0.6311000	−0.5359897	0.0494499	−0.0351862
Case 5	0.0000000	0.6683642	−0.5651308	0.0240432	−0.0153522

TABLE 1. Wavenumbers of stationary vortices for $m = 0.5$, $Re = 338$ and 2000.

vortices through the triad sum. For all the cases, the roughness modes share the same boundary value at the wall surface, and the difference of the shape functions is due to the roughness wavenumbers. Relative to the size at the wall surface, the peak values of the roughness modes are amplified significantly in the critical layer. The reason for this is that the corresponding roughness wavenumbers in the triad sum are very close to (β_s^r, α_s^r), as shown in figure 3 – that is, the roughness modes are in near-resonance with the right-branch neutral stationary eigenmode. At $Re = 338$, as the growth rate increases from case 5 to case 2, and the roughness wavenumbers (β_w, α_w) in the triad sum become closer to (β_s^r, α_s^r) (figure 3*a*,*c*), the peak values of the corresponding shape functions become larger and their vertical positions move closer to y_c, as displayed in figure 5(*a*). At $Re = 2000$, a similar trend can be observed from case 1 to case 3 (figure 5*b*), and at higher Reynolds numbers, the peak values of the roughness modes are greater in general, because the corresponding roughness wavenumbers are closer to (β_s^r, α_s^r); see figure 3(*b*,*d*).

https://doi.org/10.1017/jfm.2018.817 Published online by Cambridge University Press

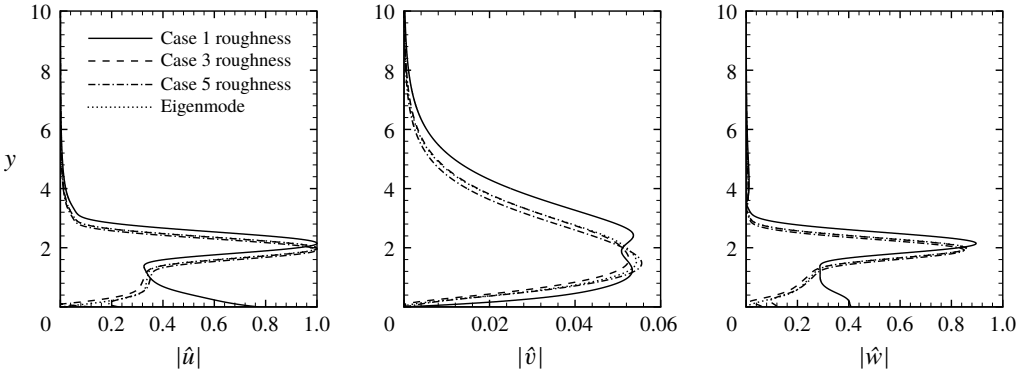


FIGURE 6. Comparison of the roughness modes in the triad sum of cases 1, 3 and 5 at $Re = 2000$ with the eigenfunction of the right-branch neutral eigenmode (β_s^r, α_s^r).

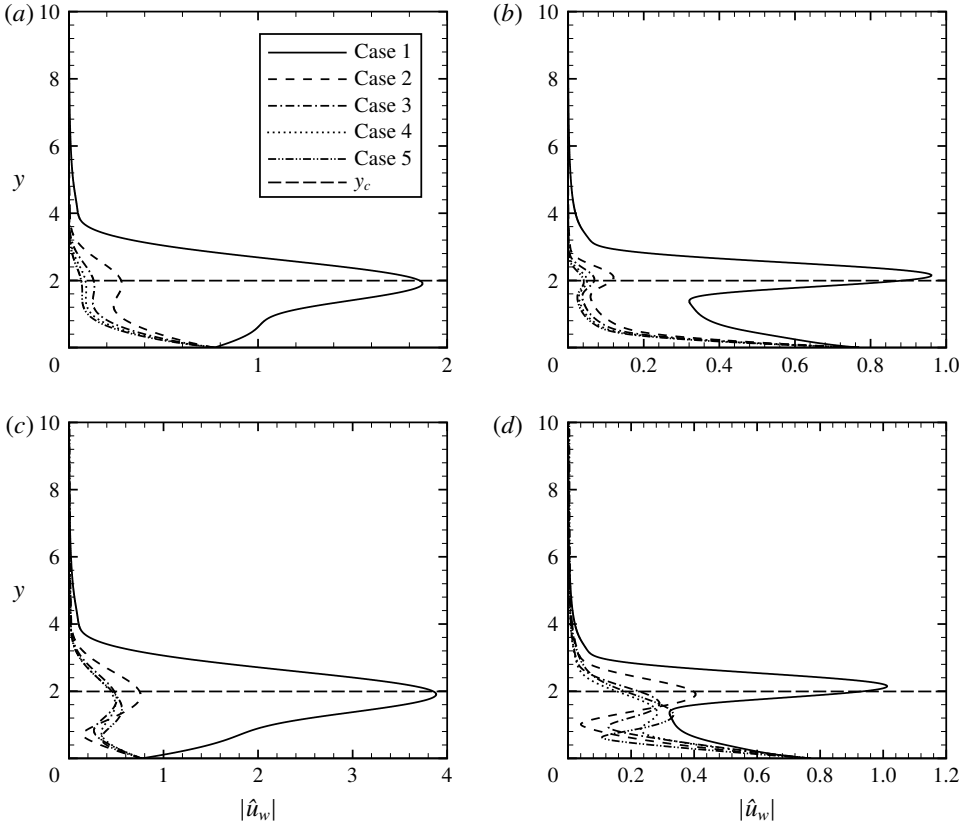


FIGURE 7. Distribution of the roughness modes in the Bragg scattering for the (*a*,*b*) right-branch and (*c*,*d*) left-branch eigenmodes: (*a*,*c*) $Re = 338$; (*b*,*d*) $Re = 2000$.

In figure 6, the shape functions of the roughness modes in the triad sum of cases 1, 3 and 5 at $Re = 2000$ are compared with those of the right-branch neutral stationary eigenmode (β_s^r, α_s^r). Note that the roughness-mode shape functions are normalized

https://doi.org/10.1017/jfm.2018.817 Published online by Cambridge University Press

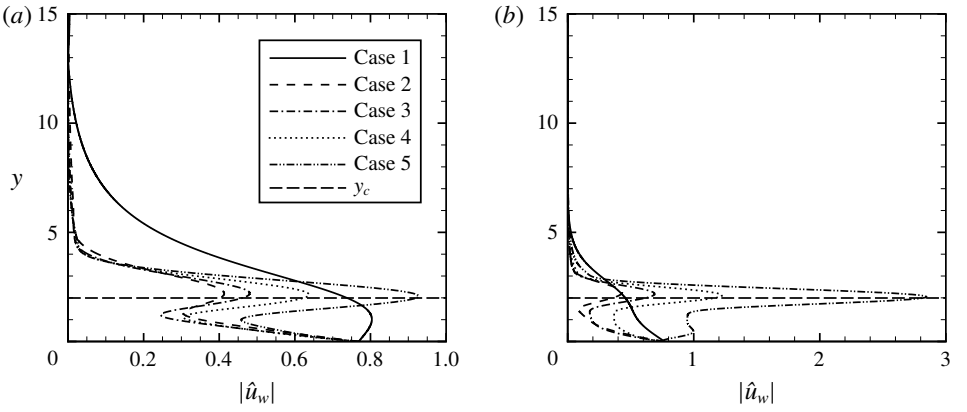


FIGURE 8. Distribution of the roughness modes in the triad difference $(1-2)$ interaction: (*a*) $Re = 338$; (*b*) $Re = 2000$.

by the maximum value of $|\hat{u}_w|$. The transverse distributions of the roughness modes almost overlap with the eigenfunction of (β_s^r, α_s^r). For case 1, where the growth rate is almost the largest, the resemblance between the shape functions is not so remarkable as that for lower growth rates. Nevertheless, in the critical layer the roughness mode is still similar to the right-branch neutral stationary eigenmode.

Figure 7 shows the roughness modes in Bragg scattering for the right-branch and left-branch stationary eigenmodes. Among the five chosen cases, only the roughness mode of case 1 exhibits a critical-layer amplification for both the right-branch and left-branch eigenmodes. The reason is that only in this case are the wavenumbers (β_w, α_w) of the roughness mode sufficiently close to (β_s^r, α_s^r); see figure 3. At $Re = 2000$, the roughness mode of case 1 in Bragg scattering displays a two-layer structure as those in the triad sum. As the growth rate decreases, the roughness wavenumbers deviate from (β_s^r, α_s^r) (figure 3), which means that the corresponding response is non-resonant. There is no critical-layer amplification for cases 2–5, but there still exists a local peak near the critical level. By comparing the maximum values of the roughness modes of case 1 in Bragg scattering at $Re = 338$ and 2000, one finds that the maximum values at a lower Reynolds number are much larger than those at a higher Reynolds number, especially for the left-branch eigenmode. Bragg scattering is therefore expected to have a greater effect on the nearly most unstable stationary vortices at lower Reynolds numbers. This will be demonstrated directly after computing the growth-rate corrections.

Figure 8 shows the shape functions of the roughness modes in the triad difference. Just as those in Bragg scattering, the roughness modes in the triad difference fall into two categories: near-resonant and non-resonant. The roughness modes of case 5 have large critical-layer amplification, and are therefore near-resonant; this is expected since their wavenumbers are very close to (β_s^r, α_s^r), as shown in figure 3. Increase of the Reynolds number leads to greater critical-layer amplification (figure 8*b*). The roughness modes in cases 1–4 are non-resonant since their wavenumbers differ appreciably from (β_s^r, α_s^r), and their shape functions do not show amplification in the critical layer.

The main difference between the triad sum and difference for the same pair of stationary vortices is the roughness mode involved. The Reynolds stresses induced by

https://doi.org/10.1017/jfm.2018.817 Published online by Cambridge University Press

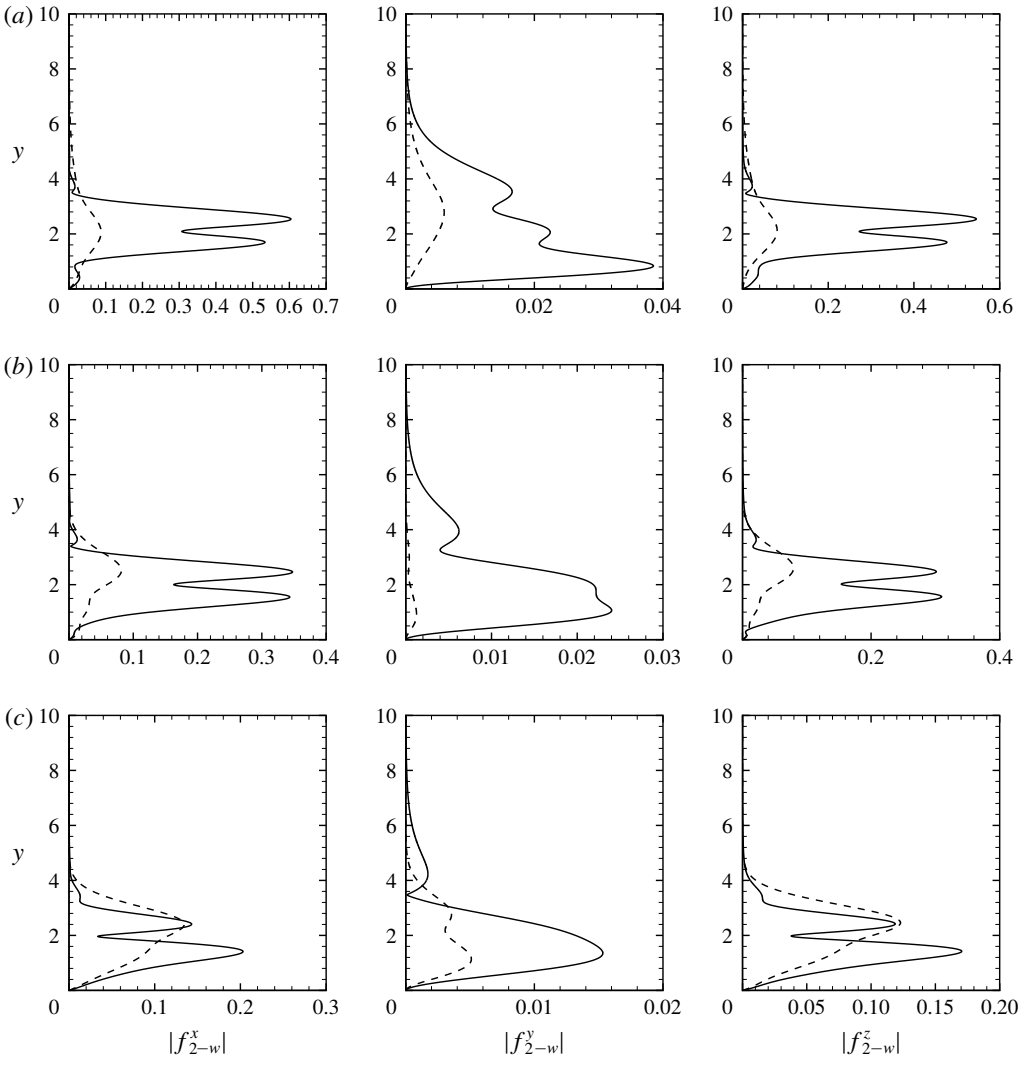


FIGURE 9. Distribution of the Reynolds stresses induced by eigenmode 2 interacting with the roughness modes at $Re = 338$: solid lines, roughness $1 + 2$; dashed lines, roughness $1 - 2$. (*a*) Case 1; (*b*) case 3; (*c*) case 5.

the interaction between the eigenmode and the roughness mode can be very different in these two mechanisms. Figure 9 presents the distribution of the Reynolds stresses induced by the eigenmodes 2 interacting with the roughness mode at $Re = 338$; the Reynolds stresses induced by the eigenmodes 1 interacting with the roughness mode exhibit similar features and are not shown. For cases 1 and 3, the Reynolds stresses in the triad sum are significantly larger than those in the triad difference. A similar feature is also observed at a higher Reynolds number $Re = 2000$; see figure 10. The huge disparity in Reynolds stresses is due to the fact that the corresponding roughness modes of cases 1 and 3 in the triad sum are near-resonant, while those in the triad difference are non-resonant. For case 5, where neutral eigenmodes are involved, the roughness modes for the triad sum and difference are both near-resonant, and so the Reynolds stresses are comparable.

https://doi.org/10.1017/jfm.2018.817 Published online by Cambridge University Press

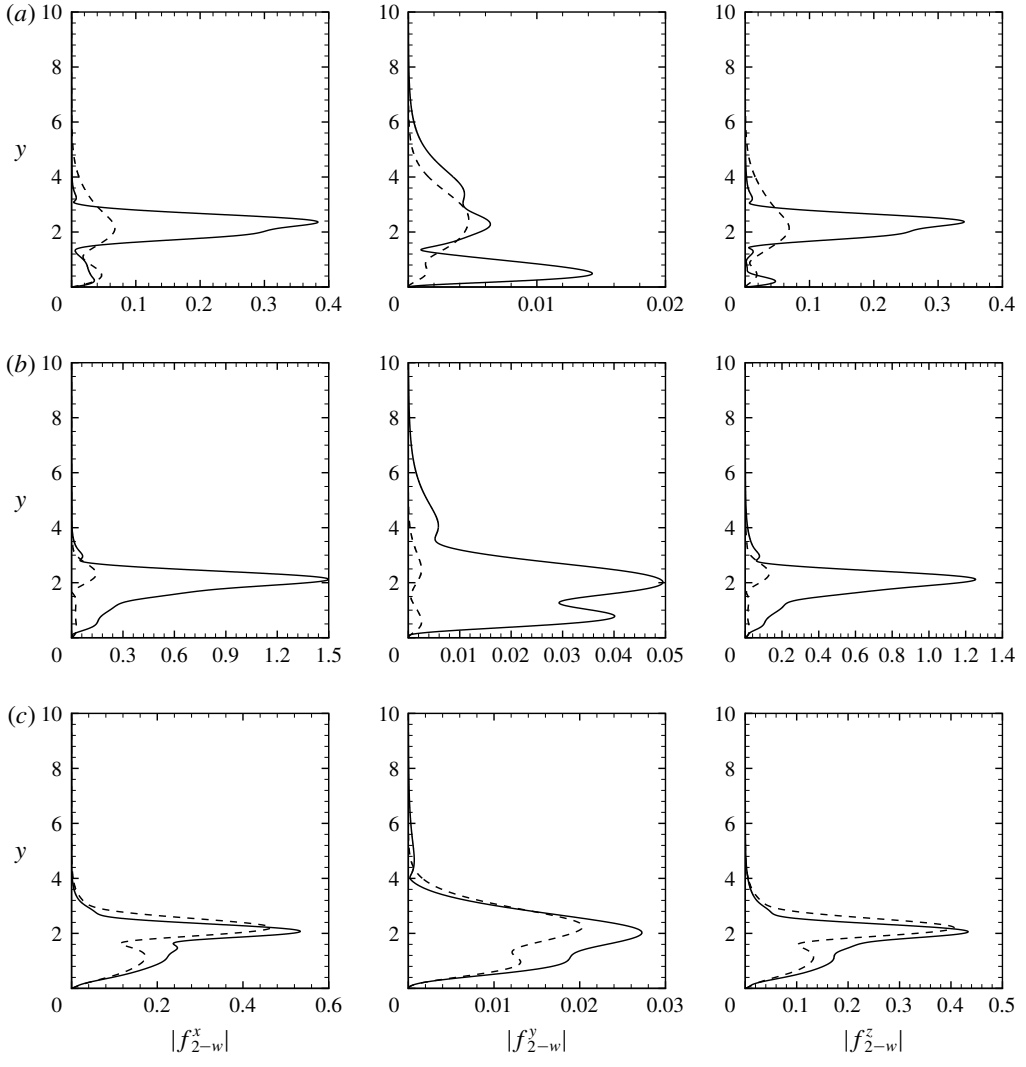


FIGURE 10. Distribution of the Reynolds stresses induced by eigenmode 2 interacting with the roughness modes at $Re = 2000$: solid lines, roughness $1 + 2$; dashed lines, roughness $1 - 2$. (*a*) Case 1; (*b*) case 3; (*c*) case 5.

Figure 11 shows the variation of the growth-rate correction coefficient λ_r with the leading-order growth rate $(-\alpha_i)$ for stationary vortices interacting with single-wavenumber roughness through Bragg scattering, triad sum and triad difference for the three acceleration parameters and two Reynolds numbers. For Bragg scattering (figure 11*a*,*b*), the curve representing the correction coefficient has two branches, because the left and right-branch modes are affected independently. The two branches merge at the maximum growth rate. The correction coefficients are larger for all left-branch modes at $Re = 338$ (figure 11*a*), but at $Re = 2000$, larger λ_r is observed for the left-branch eigenmodes with relatively large $-\alpha_i$, and this switches to the right-branch modes when $-\alpha_i$ is small (figure 11*b*). The correction coefficient is highly peaked around the maximum growth rate, acquiring much larger values there

https://doi.org/10.1017/jfm.2018.817 Published online by Cambridge University Press

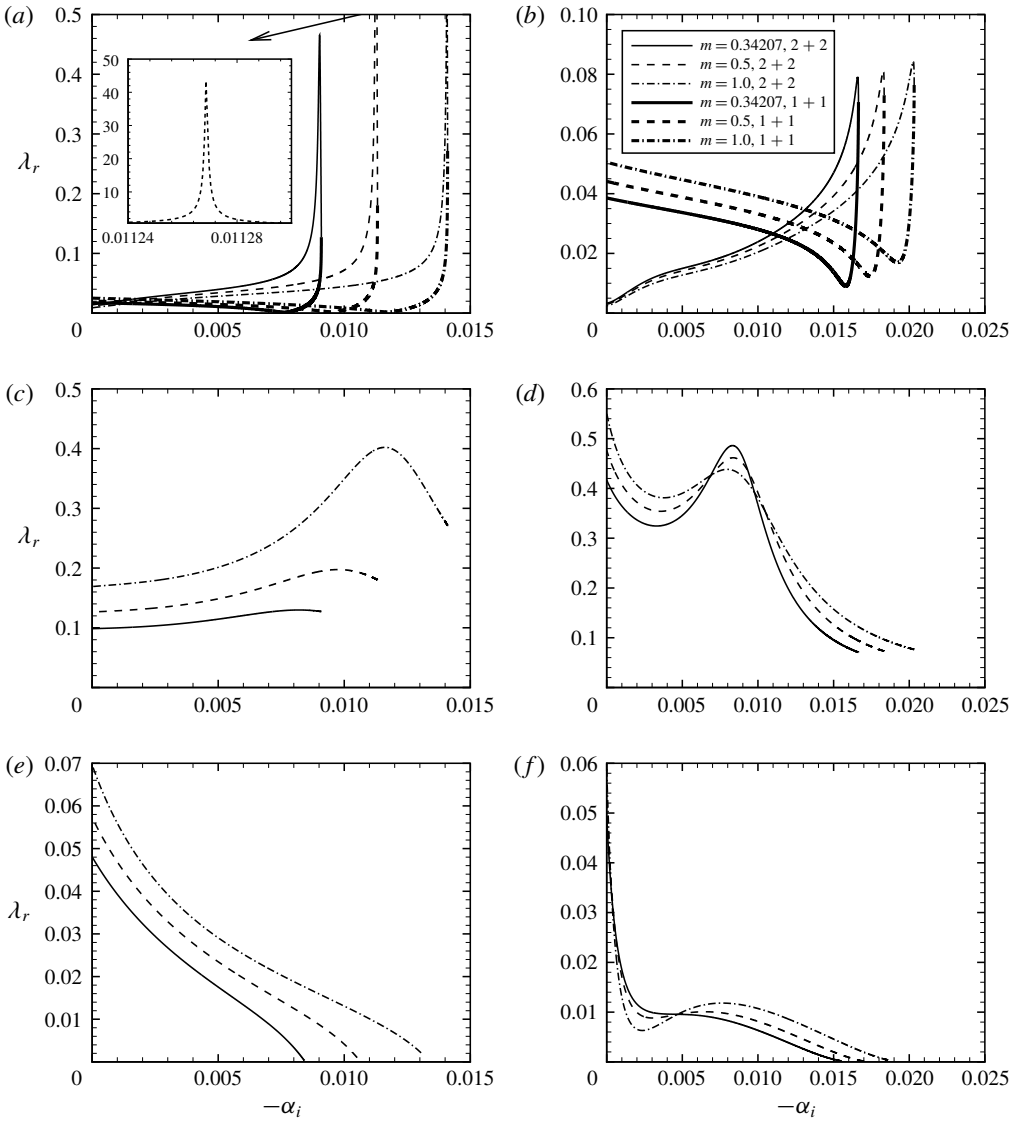


FIGURE 11. Variation of λ_r with $-\alpha_i$ for stationary vortices interacting with single-wavenumber roughness through Bragg scattering (*a*,*b*), triad sum (*c*,*d*) and triad difference (*e*,*f*). (*a*,*c*,*e*) $Re = 338$; (*b*,*d*,*f*) $Re = 2000$.

than those elsewhere because the roughness modes involved are near-resonant. This means that the most or nearly most unstable stationary vortices can become even more unstable due to Bragg scattering. At $Re = 338$, the peak value of λ_r through Bragg scattering is extremely large (approximately 45, much greater than that at $Re = 2000$). This is attributed to the fact that the corresponding roughness wavenumbers are almost equal to (β_s^r, α_s^r), and so the forcing is almost in exact resonance with the right-branch neutral stationary eigenmode. For suitable baseflow parameters and stationary eigenmode, an exact resonance may occur and Bragg scattering leads to an infinitely large λ_r, in which case the problem has to be regularized by introducing appropriate physical effects, which can be the non-parallelism of the baseflow.

https://doi.org/10.1017/jfm.2018.817 Published online by Cambridge University Press

The destabilizing effect of the Bragg scattering has implications for the application of DRE technology to delay transition. In order to suppresses the targeted most amplified stationary vortices, the spanwise wavelength of DREs is required to be smaller than that of the target mode (Saric & Reed 2003). DREs are streamwise isolated, and the control eigenmode excited is different from the 'roughness mode': the former amplifies then attenuates downstream of DREs, whereas the 'roughness mode' is sustained by extended streamwise distributed roughness, and does not undergo amplification–attenuation. The spanwise wavelength of DREs is typically taken to be 2/3 that of the target mode, in which case Bragg scattering cannot occur (Wassermann & Kloker 2002; Saric & Reed 2003). However, if DREs have twice the spanwise wavenumber of the target eigenmode, the 'control mode' excited will also have twice streamwise wavenumber because of the (nearly) linear relation between α_r and β. The Bragg scattering as described here would take place between the target and control modes in the vicinity of the location where the latter becomes neutral (like a 'roughness mode') and acquires its maximum amplitude. The consequence is an increased growth rate of the target mode. Based on these theoretical considerations, we believe that DREs with half the spanwise wavelength of the target eigenmode could potentially be counterproductive, and should better be avoided. Control modes such wavelengths were investigated by Li *et al.* (2011) and Malik *et al.* (2013) using PSE. However, no enhanced growth was observed, and the control modes still suppressed the target mode. This is rather surprising, but may be due to the fact that the control mode is in the highly nonlinear stage, where a significant spanwise uniform mean-flow distortion is generated, and acts to stabilize the target mode. The PSE computations mentioned above indeed indicate that the suppression operates in the region where the control mode has attenuated to a very low level whilst the mean-flow distortion persists. Messing & Kloker (2010) carried out a DNS study of the effect of a control mode with twice the wavenumber of the target mode, both being excited by suction through a single row of spanwise periodic and chordwise compact holes. A resonant destabilizing effect was not observed. This is most probably because in the region considered the control mode is linearly unstable ($-\alpha_i \neq 0$), and so the resonance condition is not satisfied. The nonlinearly generated mean-flow distortion again suppresses the target mode.

The correction coefficient due to the triad sum is shown in figure 11(*c*,*d*). At $Re = 338$, the correction coefficients for higher growth rates are generally larger than those for lower growth rates, whereas at $Re = 2000$ the opposite is true. The correction is rather substantial for the majority of $(-\alpha_i)$ values, which is because the roughness wavenumbers are close to (β_s^r, α_s^r). As m increases, λ_r becomes larger. Since the case with $m = 1$ is representative of the flow condition near the leading edge, the above trend is consistent with the experimental observation that roughness in that region plays a more sensitive role. Figure 11(*e*,*f*) displays the correction coefficient due to the triad difference. The correction coefficient attains its maximum at $-\alpha_i = 0$ since the roughness mode is in near-resonance with the right-branch neutral stationary crossflow vortices. For the majority of $(-\alpha_i)$ values, the correction coefficient due to the triad difference is merely of $O(10^{-2})$, while that due to the triad sum is of $O(10^{-1})$; the reason for this remarkable disparity was given above. As we will show later, the triad sum can be a very efficient mechanism, through which micron-sized distributed roughness creates a more-or-less $O(1)$ correction to the leading-order growth rate of stationary vortices.

The above results are for single-wavenumber roughness. As we noted earlier, a pair of stationary crossflow modes with equal growth rate can interact with four

https://doi.org/10.1017/jfm.2018.817 Published online by Cambridge University Press

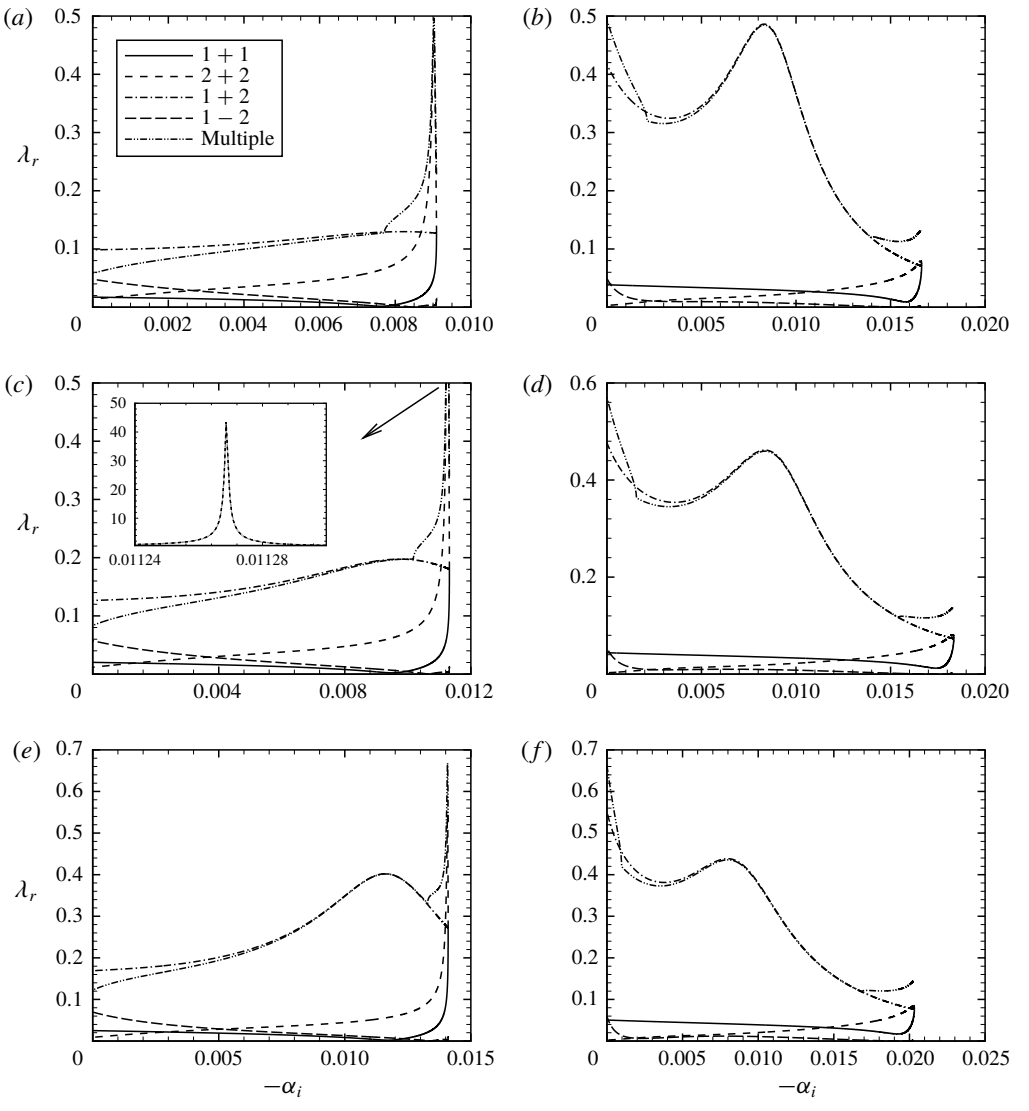


FIGURE 12. Comparisons of λ_r for stationary vortices interacting with multiple-wavenumber and single-wavenumber roughness for $m = 0.34207$ (a,b), $m = 0.5$ (c,d) and $m = 1.0$ (e,f). (a,c,e) $Re = 338$; (b,d,f) $Re = 2000$.

roughness components. Calculations were carried out for this extended case assuming that all roughness components have the same amplitude. The resulting correction coefficients are compared in figure 12 with those for single-wavenumber roughness. A main feature is that the λ_r for the multiple-wavenumber interaction is similar to that for the single-wavenumber interaction that dominates among the four interactions. At $Re = 338$, interactions $2 + 2$ and $1 + 2$ dominate at high and low growth rates, respectively; at $Re = 2000$, the dominant one is always $1 + 2$. These results indicate the special importance of Bragg scattering for stationary eigenmodes with high growth rates at low Reynolds numbers, and the strong effect of the triad sum on the majority of stationary eigenmodes. For larger m, the overall correction coefficient increases.

https://doi.org/10.1017/jfm.2018.817 Published online by Cambridge University Press

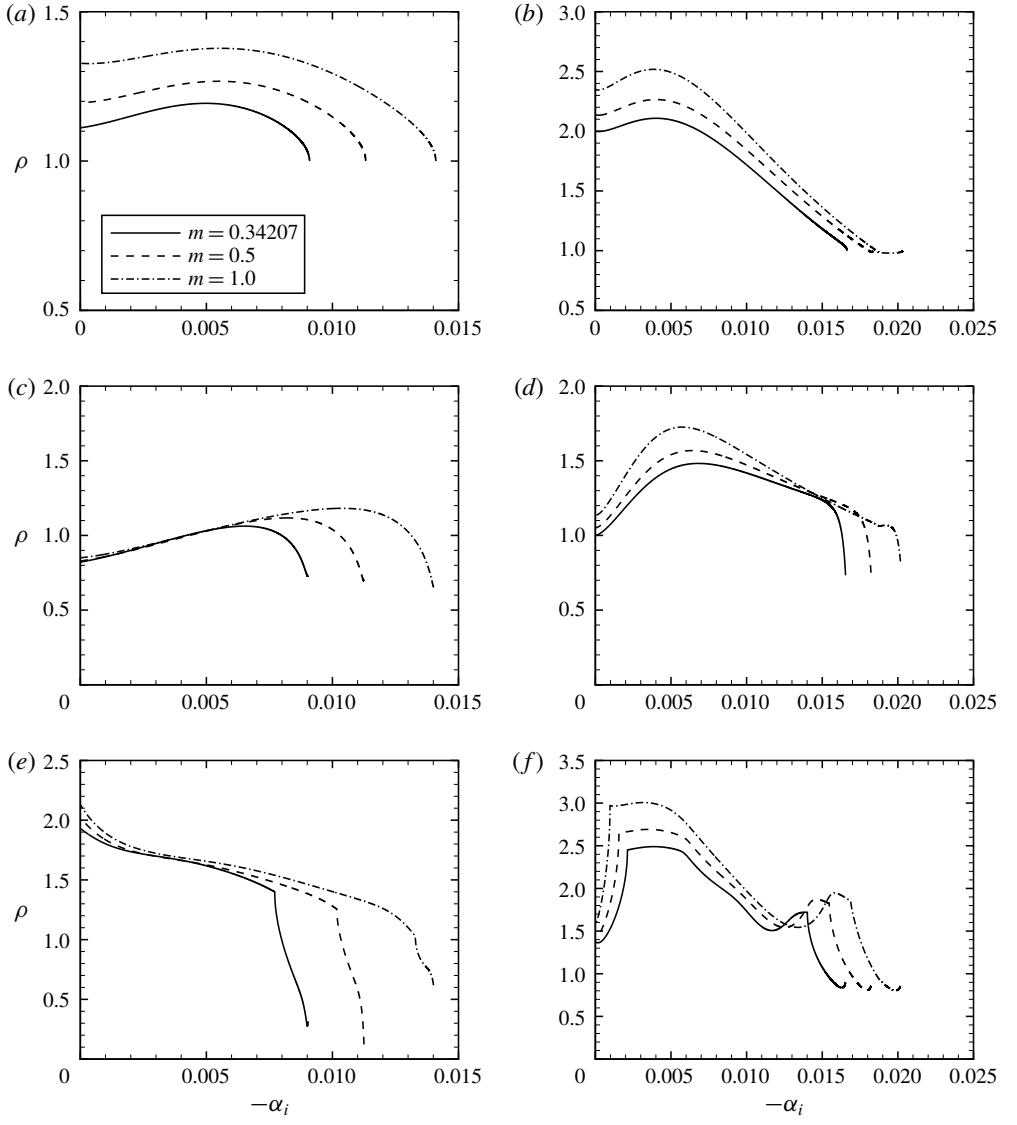


FIGURE 13. Variation of ρ with $-\alpha_i$ for stationary vortices interacting with single-wavenumber roughness through triad sum (a,b), triad difference (c,d) and with multiple-wavenumber roughness (e,f). (a,c,e) $Re = 338$; (b,d,f) $Re = 2000$.

Besides the correction to the growth rates, distributed roughness determines the amplitude ratio of the eigenmodes involved in the resonance. Figure 13 shows the amplitude ratio ρ for single-wavenumber and multiple-wavenumber roughnesses. Note that ρ is taken as the ratio of the amplitude of the right-branch eigenmode to that of the left-branch eigenmode. For the triad sum $\rho > 1$ (figure 13a,b), which means that the right-branch stationary eigenmode is stronger than its left-branch counterpart. As the acceleration parameter m increases, so does ρ. For the triad difference (figure 13c,d), the amplitude ratio at intermediate growth rates is larger than that at low and high growth rates. The amplitude ratio of stationary vortices interacting with

https://doi.org/10.1017/jfm.2018.817 Published online by Cambridge University Press

multiple-wavenumber roughness is shown in figure 13(*e*,*f*). Interestingly, although the correction coefficient is determined by the dominant interaction, ρ is not; minor interactions such as the triad difference appear to affect the amplitude ratio substantially.

4.2. *Resonant interactions of travelling vortices with roughness modes*

Four travelling crossflow eigenmodes can interact with six roughness modes with suitable wavenumbers (figure 2*a*). A parametric study is to be performed for $m = 0.34207$ and $m = 1.0$ at $Re = 338$ and 2000. As with stationary vortices, the wavenumbers of the roughness participating in the interactions are presented first with the particular attention to their 'distances' to the wavenumbers (β_s^r, α_s^r) of the right-branch neutral stationary eigenmode. Then the shape functions of the roughness modes are displayed in order to monitor their near-resonant and non-resonant nature. Finally, the results on the growth-rate correction coefficient and amplitude ratio are presented. For brevity, the results on the roughness modes are shown only for $m = 1.0$ since those for other values of m turned out to be similar.

Figure 14 shows the roughness wavenumbers in the triad sum for the four chosen frequencies of travelling vortices with $m = 1.0$ at $Re = 338$ and 2000. Among four possible triad-sum interactions, the wavenumbers of roughnesses $2 + 3$ and $1 + 4$ are fairly close to (β_s^r, α_s^r) for a considerable range of $(-\alpha_i)$, whereas those of $1 + 3$ and $2 + 4$ differ significantly from (β_s^r, α_s^r) except at the maximum growth rate, where roughnesses $1 + 3$ and $2 + 3$ have the same wavenumbers, and so do roughnesses $2 + 4$ and $1 + 4$ because eigenmodes 1 and 2 coalesce. The result suggests that the roughness modes $2 + 3$ and $1 + 4$ are mainly near-resonant, whereas $1 + 3$ and $2 + 4$ are mainly non-resonant. The interactions $2 + 3$ and $1 + 4$ are therefore of primary importance. As the Reynolds number increases, the wavenumbers of roughness $2 + 3$ become closer to (β_s^r, α_s^r). As was mentioned earlier, when the frequency of travelling vortices tends to zero roughnesses $2 + 3$ and $1 + 4$ both become the roughness $1 + 2$ for the stationary vortices, governed by the triad sum, whereas roughnesses $1 + 3$ and $2 + 4$ become $1 + 1$ and $2 + 2$, governed by Bragg scattering. The near-resonant or non-resonant nature of the roughnesses in the triad sum for travelling vortices is consistent with that for stationary vortices.

As for stationary vortices, the roughness wavenumbers (β_w, α_w) in the triad difference for the four chosen frequencies differ significantly from (β_s^r, α_s^r) except near $-\alpha_i = 0$. With the frequency increased, the roughness wavenumbers deviate substantially from (β_s^r, α_s^r) even for $-\alpha_i \approx 0$. The results are not shown in order to limit the length of the paper. The roughness modes $1 - 2$ and $3 - 4$ in the triad-difference interactions of travelling vortices are both non-resonant except for small ω and $-\alpha_i \approx 0$. It is expected that the triad-difference interactions are in general less important than the triad-sum interactions.

The shape functions of the roughness modes in the different interactions are now examined. The chosen frequencies for $Re = 338$ and 2000 are 0.035 and 0.029, respectively, which are approximately the frequencies of the corresponding most unstable travelling vortices. For each Re and ω, three cases with different growth rates are chosen; see table 2. Among these, the growth rates of eigenmodes 1 and 2 in case 1 are close to the largest, and the eigenmodes in case 3 are neutral. Figure 15 shows the roughness modes in the triad sum at $Re = 338$ and 2000. The perturbation induced by roughness $2 + 3$ is appreciably stronger than that induced by $1 + 3$. This is a consequence of the fact that the wavenumbers of roughness $2 + 3$

https://doi.org/10.1017/jfm.2018.817 Published online by Cambridge University Press

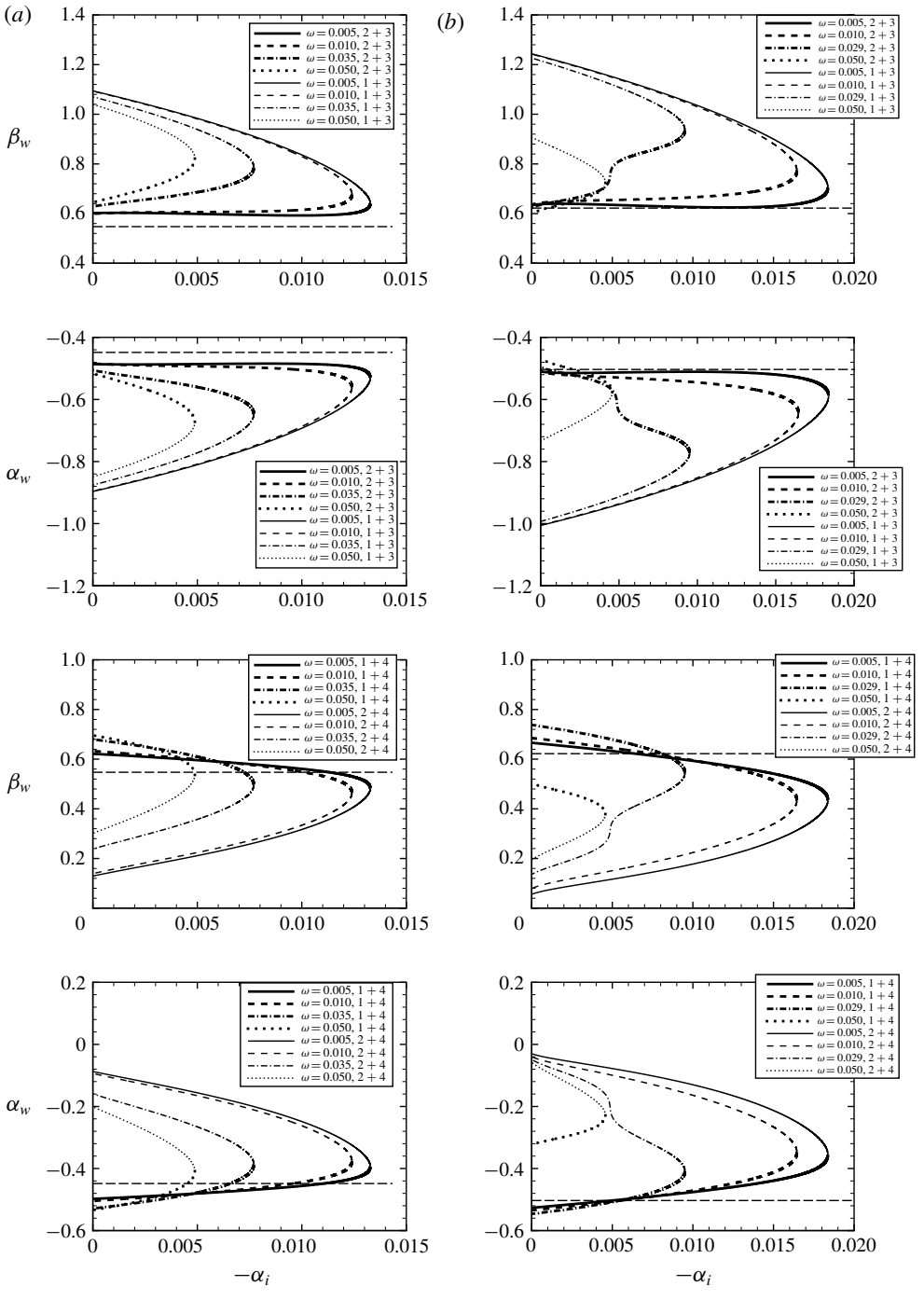


FIGURE 14. The wavenumbers of the roughness modes in the triad-sum interactions with travelling vortices for $m = 1.0$: (*a*) $Re = 338$; (*b*) $Re = 2000$. The long dashed lines stand for (β_s^r, α_s^r).

https://doi.org/10.1017/jfm.2018.817 Published online by Cambridge University Press

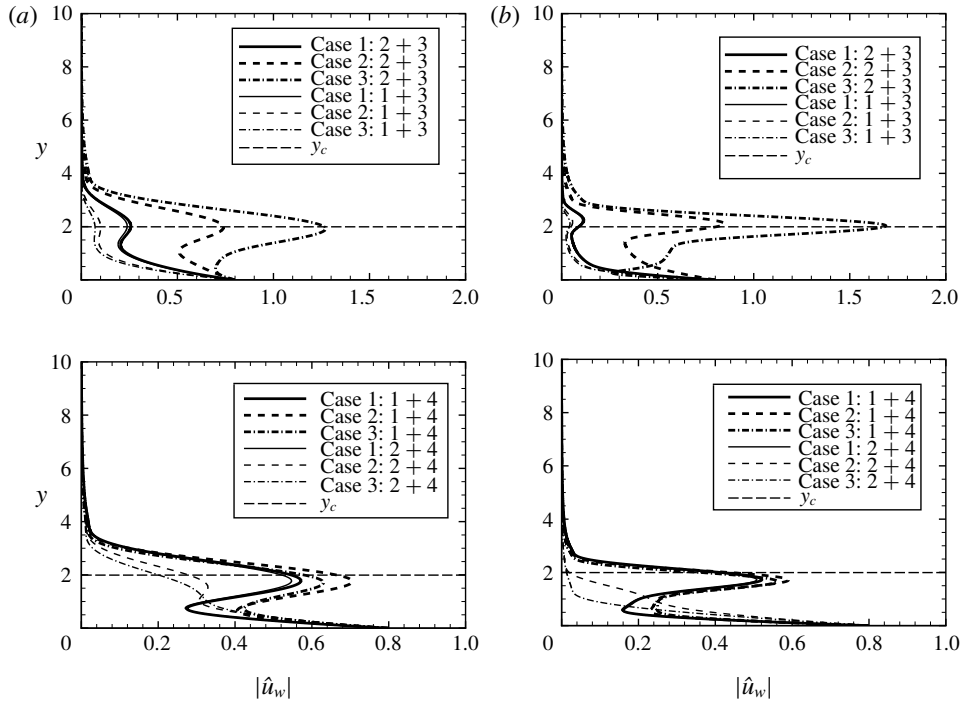


FIGURE 15. Distribution of the roughness modes in the triad-sum interactions with travelling vortices for $m = 1.0$: (*a*) $Re = 338$ and $\omega = 0.035$; (*b*) $Re = 2000$ and $\omega = 0.029$.

are closer to (β_s^r, α_s^r) than those of $1 + 3$ (figure 14). The same trend can also be found for roughnesses $1 + 4$ and $2 + 4$. There exists a local peak near the critical level y_c. As the growth rate decreases from case 1 to case 3, the peak value rises for roughness $2 + 3$ and falls for $1 + 3$; the peak value for roughness $1 + 4$ rises first and then falls, whereas that for roughness $2 + 4$ falls. These behaviours are consistent with the closeness of the roughness wavenumbers to (β_s^r, α_s^r) in the triad sum as shown in figure 14. At $Re = 2000$, the near-resonant roughness modes display high-Reynolds-number features: the two-layer structure and the larger amplifications in the critical layer.

The signature of the roughness modes in the triad-difference interactions with travelling vortices is also calculated (but not shown here). According to the sizes of the roughness modes in the critical layer, only $1 - 2$ of case 3 is near-resonant, and its peak value rises with the Reynolds number. As the growth rate increases from case 3 to case 2, the perturbation induced by roughness $1 - 2$ decreases. The perturbations induced by roughness $3 - 4$ for all three cases are all non-resonant. These results are also consistent with the 'distances' of the roughness wavenumbers (β_w, α_w) to (β_s^r, α_s^r) in the triad difference.

Figure 16 shows the growth-rate correction coefficient for travelling vortices in the triad sum and difference interactions at $Re = 338$. For a fixed frequency of eigenmodes, the correction coefficients of roughnesses $2 + 3$ and $1 + 3$ are equal at the maximum growth rate because eigenmodes 1 and 2 coalesce there. The same remarks apply to roughnesses $1 + 4$ and $2 + 4$. The correction coefficient due to roughness $2 + 3$ is larger than that due to $1 + 3$. This can be attributed to the fact

https://doi.org/10.1017/jfm.2018.817 Published online by Cambridge University Press

	ω	Case 1	Case 2	Case 3
$Re = 338$	0.035	0.0076963	0.0038529	0.0000000
$Re = 2000$	0.029	0.0094996	0.0047539	0.0000000

TABLE 2. Growth rates for the chosen cases of travelling vortices at $m = 1.0$.

that the perturbations induced by the former are larger than those induced by the latter, as shown in figure 15(*a*). For the same reason, the correction coefficient due to $1 + 4$ is larger than that due to $2 + 4$. For roughness $2 + 3$ at Travelling vortices with high frequencies, the correction coefficient due to $2 + 3$ interaction increases as the growth rate decreases. For roughness $1 + 4$ at $\omega = 0.005$, there exists a prominent peak located close to the maximum growth rate for each acceleration parameter. The corresponding roughness wavenumbers are almost equal to (β_s^r, α_s^r), as shown in figure 14(*a*), which means that the roughness mode is almost in exact resonance with the right-branch neutral stationary eigenmode. An exact resonance may take place in the non-stationary case under suitable conditions, as it does in the stationary case. The correction coefficients caused by $2 + 3$ and $1 + 4$ interactions in the triad sum are of $O(10^{-1})$, whereas those by $1 + 3$ and $2 + 4$ interactions are much smaller. The correction coefficients due to the triad difference are of $O(10^{-2})$. The reason for this significant difference is that the perturbations induced by roughnesses $2 + 3$ and $1 + 4$ are mainly near-resonant, while those induced by roughnesses $1 + 3$, $2 + 4$, $1 - 2$ and $3 - 4$ are non-resonant, as was demonstrated earlier. Overall, as m increases, so does the correction coefficient. The correction coefficient at $Re = 2000$ is shown in figure 17. The correction coefficient due to roughness $2 + 3$ for low growth rates and intermediate frequencies can be extraordinarily large, owing again to the fact that the corresponding roughness wavenumbers are close to (β_s^r, α_s^r) (figure 14*b*) and the roughness modes are amplified hugely in the critical layer (figure 15*b*). This result suggests that the leading-order growth rate cannot capture the spatial instability of travelling vortices in the presence of roughness, and the effect of roughness must be considered.

The correction coefficients for travelling vortices interacting with multiple-wavenumber and single-wavenumber roughnesses are compared in figures 18 and 19 for $Re = 338$ and 2000, respectively. The multiple-wavenumber roughness is comprised of the six Fourier components all having equal amplitude. Of the six resonant interactions, there exists a dominant one, which makes the largest contribution for each set of parameters. Broadly speaking, the dominant roughness is $2 + 3$ or $1 + 4$, each driving a perturbation in a near-resonant manner. Specifically, at $Re = 338$ the dominant single-wavenumber roughnesses are $1 + 4$ and $2 + 3$ for low and high frequencies, respectively. At a high Reynolds number ($Re = 2000$), for low frequencies ($\omega = 0.005$) there exists an intersection between the correction coefficients due to roughnesses $1 + 4$ and $2 + 3$, as shown in figure 19(*a*,*b*); roughnesses $2 + 3$ and $1 + 4$ play a dominant role at low and high growth rates respectively. For an intermediate frequency ($\omega = 0.029$) (figure 19*c*,*d*), roughness $2 + 3$ dominates at almost all growth rates. For a high frequency ($\omega = 0.05$) (figure 19*e*,*f*), the dominant single-wavenumber roughness is always $2 + 3$. The correction coefficient λ_r due to multiple-wavenumber roughness is of a similar size to that due to the dominant single-wavenumber roughness, and typically $\lambda_r = O(10^{-1})$, which implies that micron-sized roughness with multiple wavenumbers can create an $O(1)$ correction

https://doi.org/10.1017/jfm.2018.817 Published online by Cambridge University Press

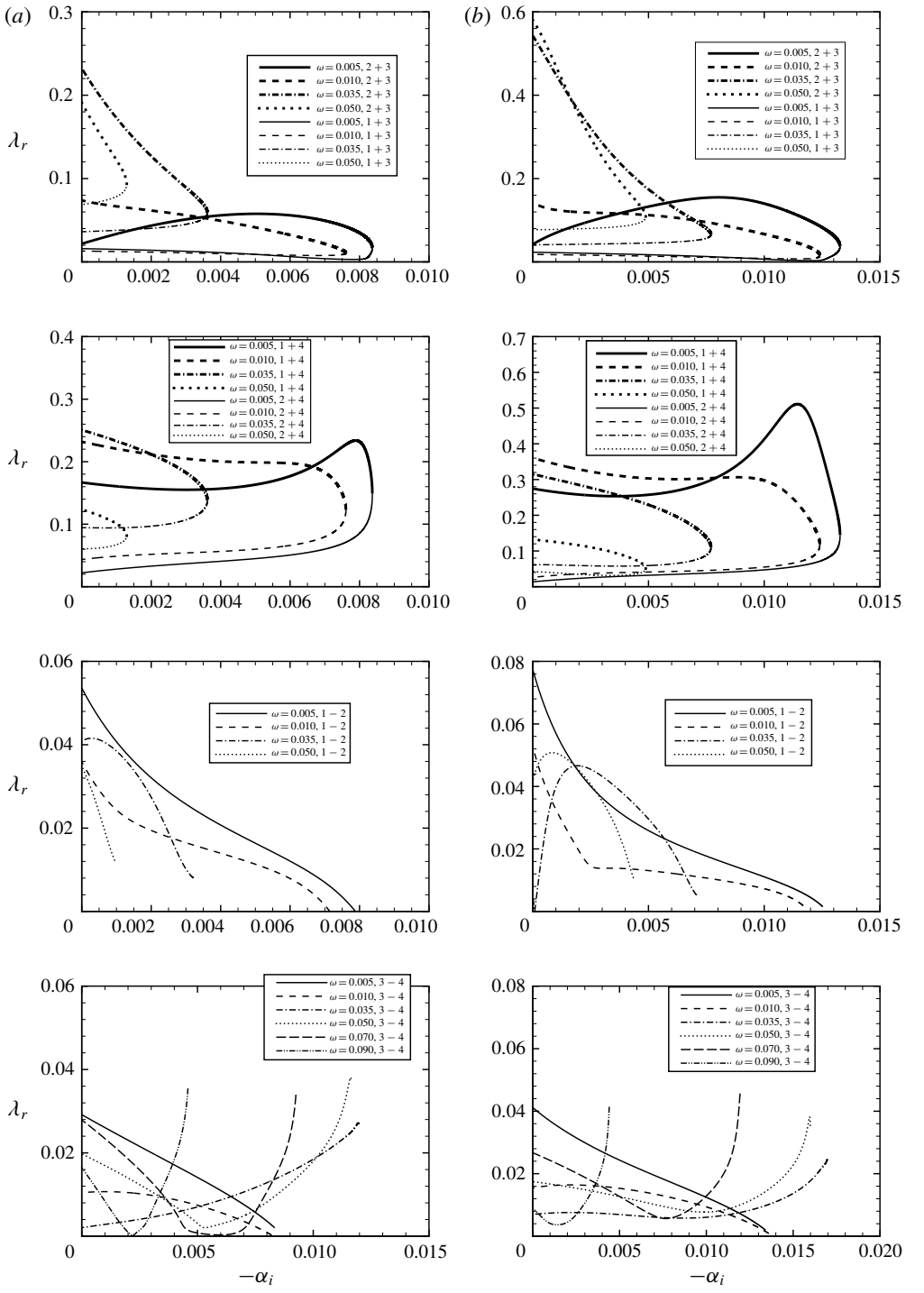


FIGURE 16. Variation of λ_r versus $-\alpha_i$ for travelling vortices of different frequency at $Re = 338$: (*a*) $m = 0.34207$; (*b*) $m = 1.0$.

https://doi.org/10.1017/jfm.2018.817 Published online by Cambridge University Press

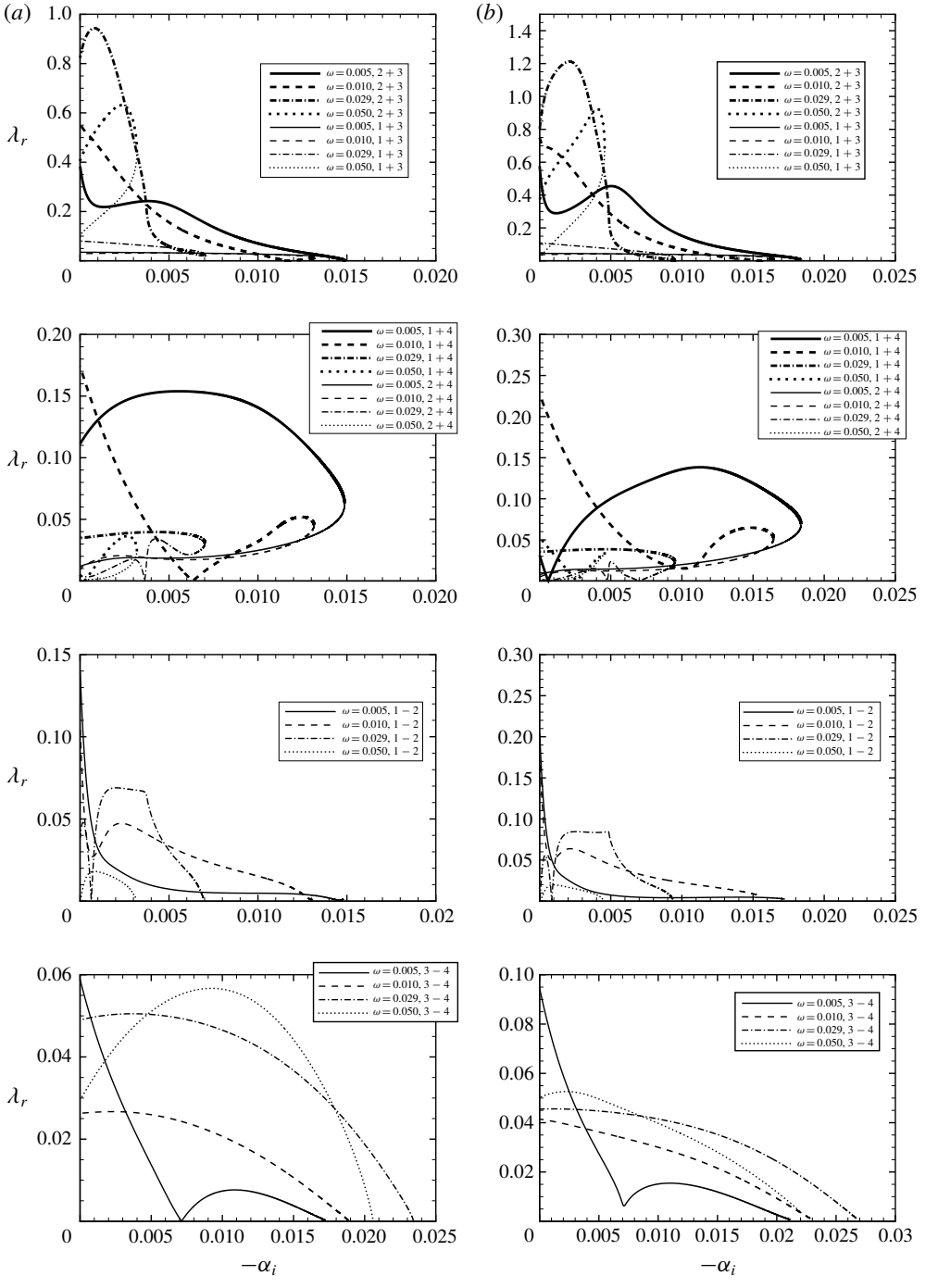


FIGURE 17. Variation of λ_r versus $-\alpha_i$ for travelling vortices of different frequency at $Re = 2000$: (*a*) $m = 0.34207$; (*b*) $m = 1.0$.

https://doi.org/10.1017/jfm.2018.817 Published online by Cambridge University Press

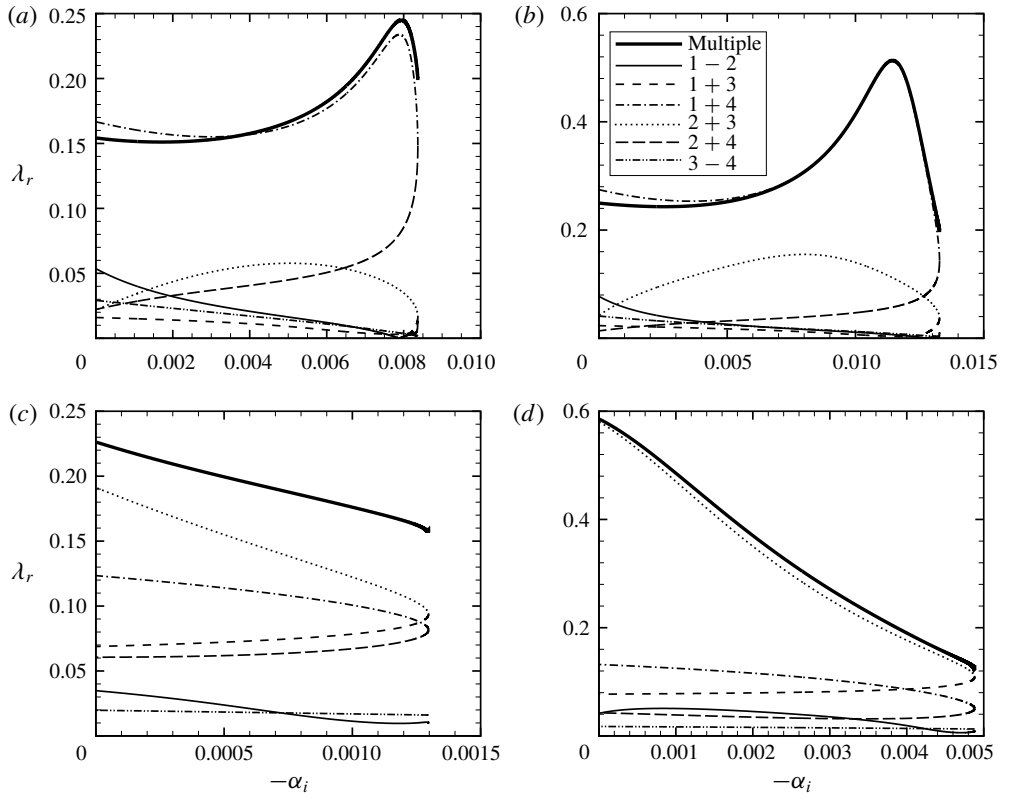


FIGURE 18. Comparisons of λ_r for travelling vortices interacting with multiple-wavenumber and single-wavenumber roughness at $Re = 338$ for $\omega = 0.005$ (a,b) and $\omega = 0.05$ (c,d). (a,c) $m = 0.34207$; (b,d) $m = 1.0$.

to the growth rates of travelling vortices, as we will show later. For larger values of m, the correction coefficient due to multiple-wavenumber roughness increases. The correction coefficient at low and high Reynolds numbers exhibits different features: for low-frequency vortices, large corrections at $Re = 338$ occur at high growth rates, while those at $Re = 2000$ occur at low growth rates; for high-frequency vortices, the correction coefficient at $Re = 338$ decreases with the growth rate, while that at $Re = 2000$ generally increases with the growth rate.

The other effect of distributed roughness on crossflow eigenmodes through the generalized resonance mechanisms is that it renders the eigenmodes involved in the resonance to obey a fixed amplitude ratio. The variation of the amplitude ratio ρ with the growth rate for travelling vortices of different frequency is shown in figure 20 for $Re = 338$ and $Re = 2000$. Note that for roughness $i + j$ or $i - j$, ρ is taken as the ratio of the amplitude of eigenmode i to that of eigenmode j. At $Re = 338$, for dominant interactions ρ takes moderate values in the range of $0.5 \leqslant \rho \leqslant 2$, but for certain non-dominant interactions, e.g. $3 - 4$, ρ can be quite large. At $Re = 2000$, ρ can be quite large as well for dominant interactions of relatively low-frequency vortices.

As noted earlier, among all possible interactions, one is dominant in the sense that it more-or-less dictates the growth-rate correction. One may ask whether the same

https://doi.org/10.1017/jfm.2018.817 Published online by Cambridge University Press

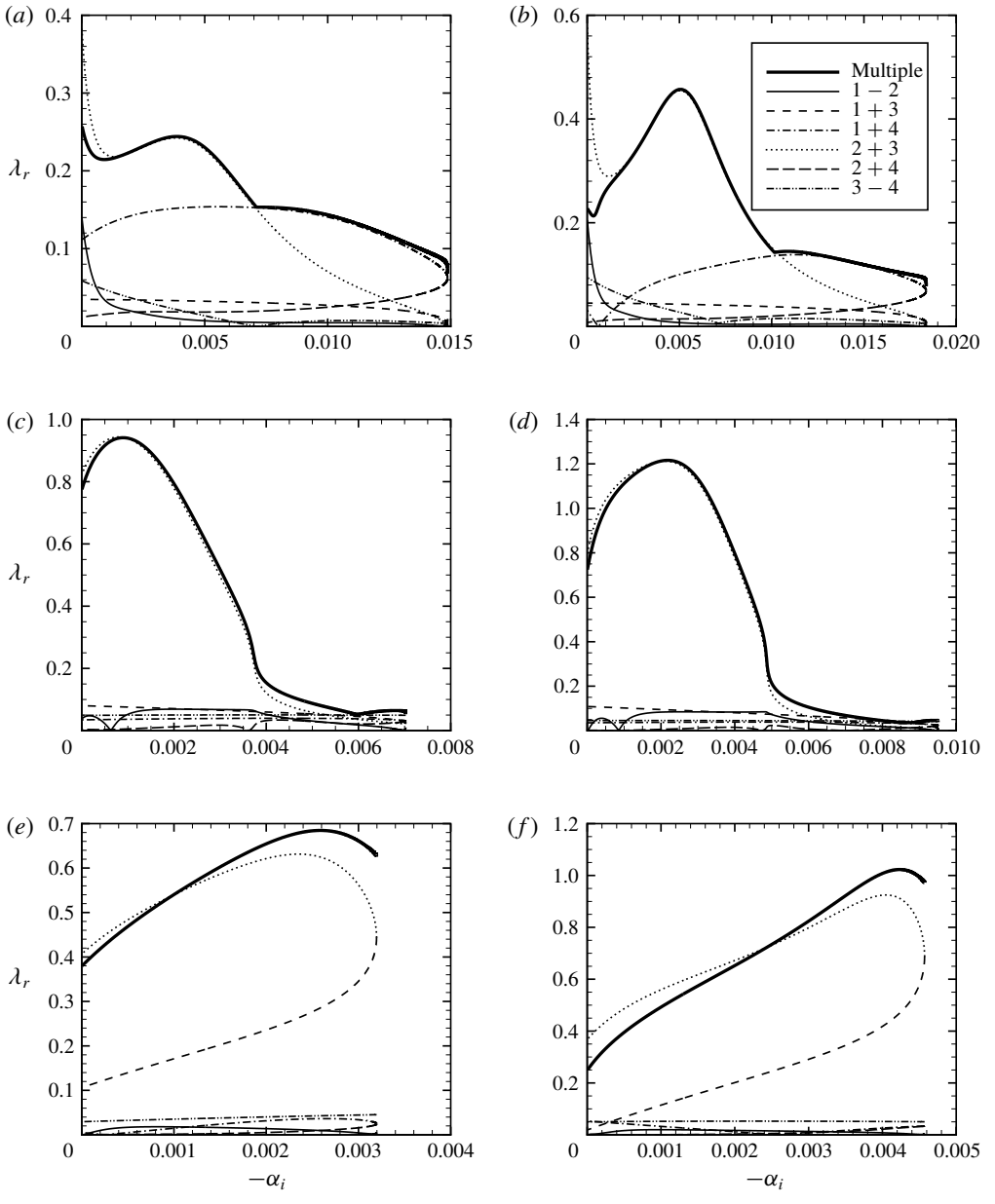


FIGURE 19. Comparisons of λ_r for travelling vortices interacting with multiple-wavenumber and single-wavenumber roughness at $Re = 2000$ for $\omega = 0.005$ (a,b), $\omega = 0.029$ (c,d) and $\omega = 0.05$ (e,f). (a,c,e) $m = 0.34207$; (b,d,f) $m = 1.0$.

behaviour extends to the amplitude ratio. This question is answered in figure 21 for $Re = 338$ and 2000. At $Re = 338$, ρ in the multiple-wavenumber case follows that in the single-wavenumber case for low frequencies at high growth rates and for high frequencies at low growth rates. At $Re = 2000$, there is a close agreement. The discontinuity of ρ with the growth rate for $\omega = 0.005$ (figure 21b) occurs where the dominant interaction changes as shown in figure 19(a,b). Therefore, we can conclude

https://doi.org/10.1017/jfm.2018.817 Published online by Cambridge University Press

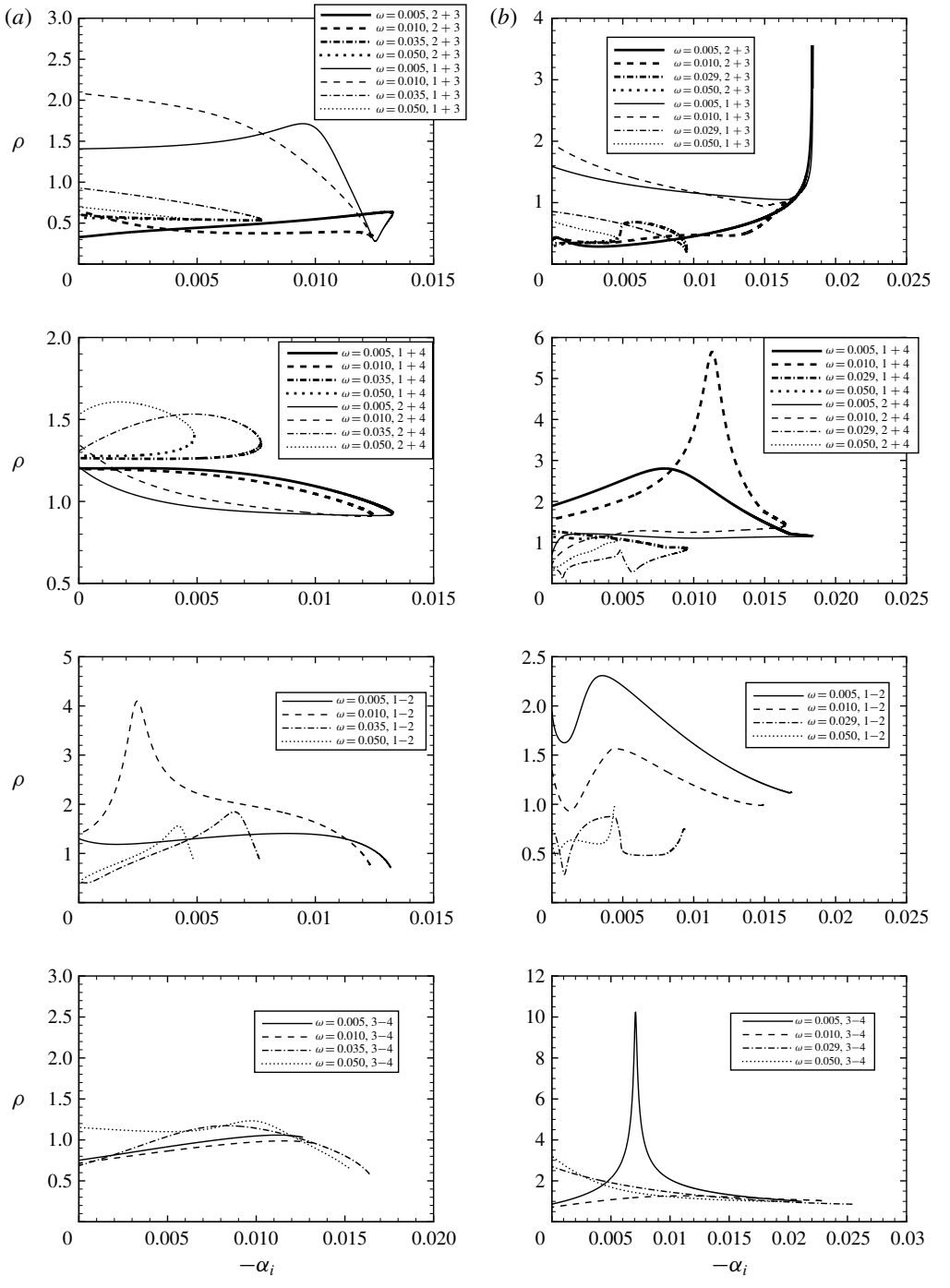


FIGURE 20. Variation of ρ versus $-\alpha_i$ for travelling vortices of different frequency at $m = 1.0$: (*a*) $Re = 338$; (*b*) $Re = 2000$.

https://doi.org/10.1017/jfm.2018.817 Published online by Cambridge University Press

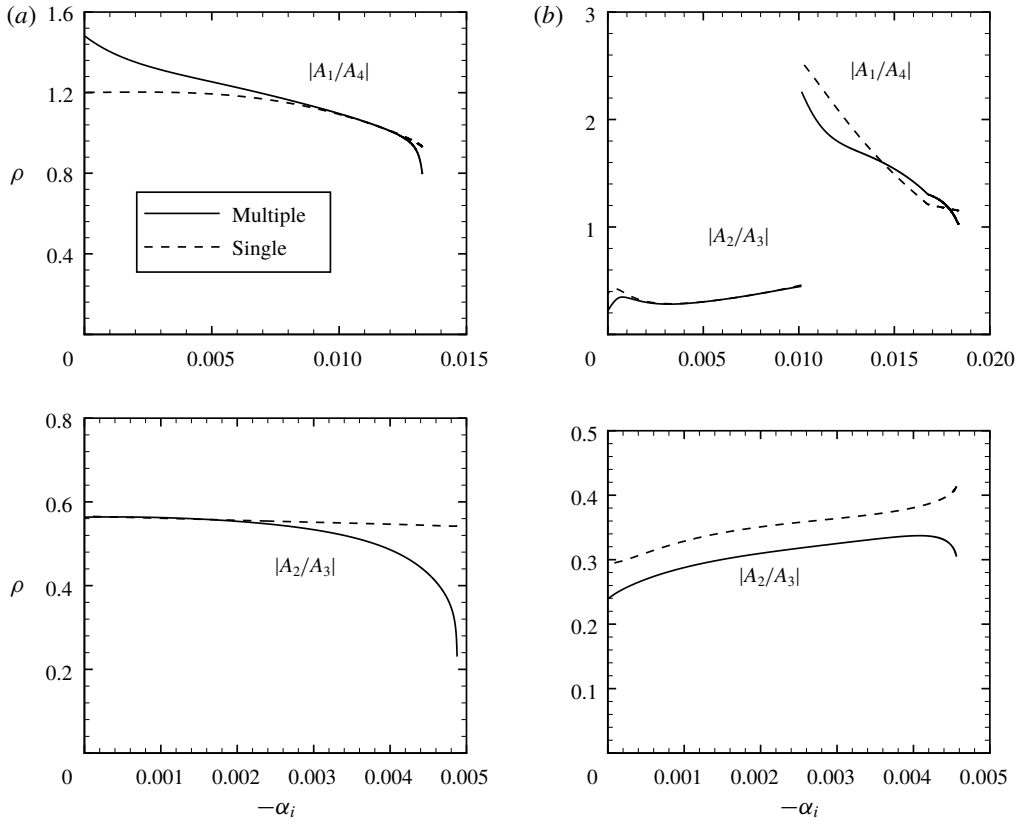


FIGURE 21. Comparison of the amplitude ratio in the multiple-wavenumber case with that in the dominant single-wavenumber case at $m = 1.0$ for $\omega = 0.005$ (a,b) and $\omega = 0.05$ (c,d). (a,c) $Re = 338$; (b,d) $Re = 2000$.

that in the multiple-wavenumber case, generally there exists a dominant interaction in the sense that the corresponding growth-rate correction coefficient and amplitude ratio are both marginally affected by other roughness components.

Our numerical results show that the growth-rate correction coefficient λ_r caused by the resonant interactions between the crossflow eigenmodes and roughness modes is approximately 0.3 in the majority of the parameter space. The correction to the leading-order growth rate is $\lambda_r h$ with $h = h^*/\delta_0^*$. The typical value of h for a micron-sized roughness is now estimated by referring to the experimental data of Radeztsky *et al.* (1999). In their experiment, a 12 μm isolated roughness element was placed at $x^*/c^* = 0.023$, and the non-dimensionalized height is defined as $h^*/\delta_{0.99}^* = 0.014$ with $\delta_{0.99}^*$ representing the transverse position where $U = 0.99$. It follows that $h^*/\delta_0^* = (h^*/\delta_{0.99}^*)y_{0.99}$, where $y_{0.99} = \delta_{0.99}^*/\delta_0^*$ is given by $U(y_{0.99}) = 0.99$. Since $x^*/c^* = 0.023$ is fairly close to the leading edge, the local boundary layer can be approximated by the FSC solution with $m = 1.0$. For the FSC boundary layer with $m = 1.0$, our computation gives $y_{0.99} = 3.6725$, and hence $h^*/\delta_0^* = 0.0514$ and $\delta_0^* = 0.2334$ mm. The chord Reynolds number $Re_c = U_{\infty,s}^* c^*/\nu^* = 2.6 \times 10^6$, where $U_{\infty,s}^*$ is the streamwise free-stream velocity, and the airfoil chord length $c^* = 1.83$ m (Carrillo *et al.* 1997). The sweep angle in the experiment is set to

https://doi.org/10.1017/jfm.2018.817 Published online by Cambridge University Press

45°. The Reynolds number based on δ_0^* at $x^*/c^* = 0.023$ is therefore estimated as $Re = (Re_c\delta_0^*)/(\sqrt{2}c^*) = 234.5$, fairly close to the low Reynolds number (338) in our computation. The Reynolds number would be equal if the roughness is present somewhat downstream where $\delta_0^* = 0.2334 \times 338/234.5 \approx 0.34$ mm. Hence, the relative height ($h = h^*/\delta_0^*$) of the micron-sized roughness (typically $h^* \approx 10$ μm for unpolished surfaces) at the lower Reynolds number ($Re = 338$) in the experimental setting is approximately 0.03. The correction to the growth rate of both stationary and travelling vortices is roughly 0.01, which is comparable to the leading-order growth rates ($O(10^{-2})$).

5. Conclusions and future work

The present paper is concerned with high sensitivity of transition in three-dimensional boundary layers to micron-sized distributed roughness. Much of the existing work sought to explain this phenomenon from the perspectives of the receptivity process and local instability of the modified baseflow. Here, a possible additional mechanism was provided by studying the effect of distributed surface roughness on crossflow instability through resonant interactions between crossflow eigenmodes and the roughness-induced perturbations. With the latter being represented as a superposition of different Fourier components, we identified several resonances which can take place between one or more growing eigenmodes and suitable roughness components to affect the growth rate of crossflow vortices. These include Bragg scattering involving a stationary eigenmode and a roughness mode, and resonant-triad interactions between two eigenmodes and a roughness component. The latter may take two forms: triad sum and triad difference, which refer to the cases where the sum/difference of the wavenumbers of the eigenmodes is equal to those of the roughness, respectively. The present Bragg scattering and resonant-triad interactions are generalized in that the eigenmodes have $O(1)$ growth rates. For the triadic interactions, all that is required is that the two eigenmodes must have equal growth rate. Owing to the resonant nature of the interactions, the correction to the growth rate is proportional to the roughness height and the scaling factor is defined as the growth-rate correction coefficient. By a multiscale method, we derive the amplitude equations of the crossflow eigenmodes interacting with distributed surface roughness through the generalized resonance mechanisms. After solving the amplitude equations, we obtained the growth-rate correction coefficient λ_r and amplitude ratio ρ of the participating eigenmodes in the resonances. The fact that the amplitude ratio ρ is fixed by roughness means that the eigenmodes in the resonance are fully coupled at the leading order; this is in stark contrast to the smooth-wall case, where eigenmodes in the linear regime are independent of each other, with their amplitude ratio being arbitrary. An important implication is that the spectral composition of crossflow vortices in a 3D boundary layer is affected by distributed surface roughness.

The size of λ_r depends on the 'distance' between the roughness wavenumbers (β_w, α_w) and the wavenumbers (β_s^r, α_s^r) of the right-branch neutral stationary eigenmode, and the roughness modes can be categorized as being near-resonant if the 'distance' is small and non-resonant otherwise. The numerical results for the FSC boundary layer indicate that, for a fairly wide range of parameters, the roughness wavenumbers satisfying one of the resonance conditions turn out to be close to (β_s^r, α_s^r), leading to a substantial correction to the growth rate. The corresponding length scales might be what Radeztsky *et al.* (1999) referred to as 'dangerous scales' that distributed roughnesses seemed to have. The numerical evaluations show that

https://doi.org/10.1017/jfm.2018.817 Published online by Cambridge University Press

at moderate Reynolds numbers the nearly most unstable stationary vortices are most sensitive to roughness through Bragg scattering. The growth-rate correction coefficient due to the triad sum for stationary vortices is generally larger than that due to the triad difference because the participating roughness mode is near-resonant in the former but non-resonant in the latter. For travelling vortices, two triad-sum interactions were found to be of primary importance in the respective ranges of the parameters. Multiple-wavenumber roughness, which is more realistic than its single-wavenumber counterpart, produces correction coefficients similar to what the dominant single-wavenumber roughness does. In the majority of the parameter space, the growth-rate correction coefficient is approximately 0.3, which suggests that roughness with 10 μm height could potentially induce a more-or-less $O(1)$ correction to the leading-order growth rates of both stationary and travelling vortices at typical Reynolds numbers where the boundary-layer displacement thickness is approximately 1 mm. The generalized resonant interactions therefore appear to be powerful mechanisms that accelerate transition. They add to the existing mechanisms of receptivity and alteration to the local instability, all of which probably operate to cause the experimentally observed high sensitivity of three-dimensional boundary-layer transition to micron-sized roughness.

The mechanisms identified in the present paper are promising enough that further work on them is warranted. It is of interest to investigate the resonant interactions in realistic three-dimensional boundary layers over swept wings. We believe that the same mechanisms operate and remain significant there, given the fact that the existence of the resonant interactions relies upon only the generic feature of the dispersion relation of crossflow instability, and their effects are significant for different values of the acceleration parameter in the FSC family, as was demonstrated in the present paper.

In the present paper, a local parallel-flow approximation is made, which suffices for the purpose of identifying the exact resonances and assessing their impact on the growth rate at each chordwise location. What remains to be studied is the non-parallel-flow effect. A pair of modes with fixed spanwise wavelengths could only satisfy the resonant conditions strictly at one chordwise location, say x_0. Away from x_0, detuning occurs and the resonant effect weakens as the baseflow and the dispersion relation vary. The non-parallelism is a rather common issue arising in other forms of wave resonances in a spatially developing baseflow, including the familiar resonant-triad interactions of T–S waves (Craik 1971; Borodulin *et al.* 2002). Since the baseflow varies slowly in the chordwise direction, the resulting detuning can be taken into account by a multiscale approach. With the extended theory, we will be able to calculate the growth-rate correction at each location for a fixed set of vortices, and also to trace their downstream development, thereby assessing more realistically the effect of the resonant interactions. We have assumed that all Fourier components in the surface roughness have constant heights, which allows the system of the amplitude equations to be reduced to an eigenvalue problem, but the analysis can be extended to roughnesses whose heights are modulated in space (that is, are functions of $\bar{x} = hx$), for which the amplitude equations would have non-constant coefficients, and will have to be investigated as an initial-value problem.

It was demonstrated that micron-sized roughness can potentially alter the growth rate by an $O(1)$ amount, but one might question whether the perturbation method used would remain appropriate when the correction is no longer small. Direct numerical simulations may thus be necessary. It is of interest to note that a DNS study of the effect of steady distributed suction, which plays a similar role as distributed

https://doi.org/10.1017/jfm.2018.817 Published online by Cambridge University Press

roughness does, was performed by Messing & Kloker (2010). The arrays of the suction holes have spanwise wavenumber twice that of the targeted eigenmode, but the chordwise wavenumber is appreciably greater than twice that of the targeted mode, and also larger than that of the right-branch neutral mode, which means that the roughness mode is neither in the subharmonic (Bragg) resonance with the targeted mode nor in the fundamental resonance with the right-branch neutral mode. Stronger growth is therefore not expected there. The work serves a useful guidance for future DNS investigation of resonant interactions, in which case the wavenumbers of the roughness element (or suction hole) pattern and the participating crossflow modes must be chosen to satisfy the resonant conditions. Finally, in the present paper the crossflow vortices are assumed linear, whereas effects of distributed roughness on nonlinear vortices await to be studied. We hope that the present theoretical results and the planned further work would prompt experimental efforts to quantify the effects of distributed roughness as well as the relative importance of different mechanisms.

Acknowledgements

The computer code used for the present work was developed from the one generously supplied by late Professor J. S. Luo of Tianjin University. X.W. would like to thank Professor W. S. Saric and Dr M. Choudhari for helpful discussions on the role of surface roughness in three-dimensional boundary-layer transition. The referees are thanked for their helpful comments and suggestions. This work was supported by The National Key Research and Development Program of China; 2016YFA0401200, and A.B. was supported by the UK EPSRC project LFC-UK (grant EP/I037946/1) and by an EPSRC Doctoral Prize Fellowship.

REFERENCES

BERTOLOTTI, F. P. 2000 Receptivity of three-dimensional boundary-layers to localized wall roughness and suction. *Phys. Fluids* **12** (7), 1799–1809.

BORODULIN, V. I., KACHANOV, Y. S. & KOPTSEV, D. B. 2002 Experimental study of resonant interactions of instability waves in a self-similar boundary layer with an adverse pressure gradient: III. Broadband disturbances. *J. Turbul.* **3** (64), 1–19.

BUTLER, A. & WU, X. 2018*a* Stationary crossflow vortices near the leading edge of three-dimensional boundary layers: the role of non-parallelism and excitation by surface roughness. *J. Fluid Mech.* **845**, 93–140.

BUTLER, A. & WU, X. 2018*b* Vortex-roughness interactions in three-dimensional boundary layers (in preparation).

CABAL, A., SZUMBARSKI, J. & FLORYAN, J. M. 2002 Stability of flow in a wavy channel. *J. Fluid Mech.* **457**, 191–212.

CARPENTER, A., SARIC, W. S. & REED, H. L. 2008 Laminar flow control on a swept wing with distributed roughness. *AIAA Paper* 2008-7335.

CARPENTER, A. L., SARIC, W. S. & REED, H. L. 2009 In-flight receptivity experiments on a 30-degree swept-wing using micron-sized discrete roughness elements. *AIAA Paper* 2009-0590.

CARRILLO, R. B. JR., REIBERT, M. S. & SARIC, W. S. 1997 Distributed-roughness effects on stability and transition in swept-wing boundary layers. *NASA Tech. Rep.* NASA-CR-203580.

CEBECI, T. & EGAN, D. A. 1989 Prediction of transition due to isolated roughness. *AIAA J.* **27** (7), 870–875.

CHOUDHARI, M. 1994 Roughness-induced generation of crossflow vortices in three-dimensional boundary layers. *Theor. Comput. Fluid Dyn.* **6** (1), 1–30.

CHOUDHARI, M. 1995 Long-wavelength asymptotics of unstable crossflow modes, including the effect of surface curvature. *Proc. R. Soc. Lond.* A **451**, 515–541.

https://doi.org/10.1017/jfm.2018.817 Published online by Cambridge University Press

CHOUDHARI, M. & DUCK, P. W. 1996 Nonlinear excitation of inviscid stationary vortex in a boundary-layer flow. *NASA Tech. Rep.* NASA-CR-198327.

COLLIS, S. S. & LELE, S. K. 1999 Receptivity to surface roughness near a swept leading edge. *J. Fluid Mech.* **380**, 141–168.

CORKE, T. C., BAR-SERVER, A. & MORKOVIN, M. V. 1986 Experiments on transition enhancement by distributed roughness. *Phys. Fluids* **29** (10), 3199–3213.

CRAIK, A. D. D. 1971 Non-linear resonant instability in boundary layers. *J. Fluid Mech.* **50** (2), 393–413.

CROUCH, J. 1993 Receptivity of three-dimensional boundary layers. *AIAA Paper* 1993-0074.

FLORYAN, J. M. 1997 Stability of wall-bounded shear layers in the presence of simulated distributed surface roughness. *J. Fluid Mech.* **335**, 29–55.

FLORYAN, J. M. 2002 Centrifugal instability of Couette flow over a wavy wall. *Phys. Fluids* **14** (1), 312–322.

GAO, B., PARK, D. H. & PARK, S. O. 2011 Stability analysis of a boundary layer over a hump using parabolized stability equations. *Fluid Dyn. Res.* **43** (5), 055503.

GASTER, M. 2016 Understanding the effects of surface roughness on the growth of disturbances. *AIAA Paper* 2016-4384.

GOLDSTEIN, M. E. & HULTGREN, L. S. 1989 Boundary-layer receptivity to long-wave free-stream disturbances. *Annu. Rev. Fluid Mech.* **21** (1), 137–166.

HAMED, A. M., SADOWSKI, M., ZHANG, Z. & CHAMORRO, L. P. 2016 Transition to turbulence over 2D and 3D periodic large-scale roughnesses. *J. Fluid Mech.* **804**, R6.

HOSSEINI, S. M., TEMPELMANN, D., HANIFI, A. & HENNINGSON, D. S. 2013 Stabilization of a swept-wing boundary layer by distributed roughness elements. *J. Fluid Mech.* **718**, R1.

HÖGBERG, M. & HENNINGSON, D. S. 1998 Secondary instability of cross-flow vortices in Falkner–Skan–Cooke boundary layers. *J. Fluid Mech.* **368**, 339–357.

HUANG, Z. & WU, X. 2017 A local scattering approach for the effects of abrupt changes on boundary-layer instability and transition: a finite-Reynolds-number formulation for isolated distortions. *J. Fluid Mech.* **822**, 444–483.

KLEBANOFF, P. S. & TIDSTROM, K. D. 1972 Mechanism by which a two-dimensional roughness element induces boundary-layer transition. *Phys. Fluids* **15** (7), 1173–1188.

KURZ, H. B. E. & KLOKER, M. J. 2014 Receptivity of a swept-wing boundary layer to micron-sized discrete roughness elements. *J. Fluid Mech.* **755**, 62–82.

LESSEN, M. & GANGWANI, S. T. 1976 Effect of small amplitude wall waviness upon the stability of the laminar boundary layer. *Phys. Fluids* **19** (4), 510–513.

LI, F., CHOUDHARI, M., CHANG, C.-L., STREETT, C. & CARPENTER, M. 2011 Computational modelling of roughness-based laminar flow control on a subsonic swept wing. *AIAA J.* **49**, 520–529.

MALIK, M. R. 1990 Numerical methods for hypersonic boundary layer stability. *J. Comput. Phys.* **86** (2), 376–413.

MALIK, M., LIAO, W., LI, F. & CHOUDHARI, M. 2013 DRE-enhanced swept-wing natural laminar flow at high Reynolds numbers. *AIAA Paper* 2013-0412.

MASAD, J. A. 1996 Effect of surface waviness on transition in three-dimensional boundary-layer flow. *NASA Tech. Rep.* NASA-CR-201641.

MASAD, J. A. & IYER, V. 1994 Transition prediction and control in subsonic flow over a hump. *Phys. Fluids* **6** (1), 313–327.

MAMUN, M. D., ASAI, M. & INASAWA, A. 2014 Effects of surface corrugation on the stability of a zero-pressure-gradient boundary layer. *J. Fluid Mech.* **741**, 228–251.

MEDEIROS, M. A. F. & GASTER, S. 1999 The production of subharmonic waves in the nonlinear evolution of wavepackets in boundary layers. *J. Fluid Mech.* **399**, 301–318.

MEI, C. C. 1985 Resonant reflection of surface water waves by periodic sandbars. *J. Fluid Mech.* **152**, 315–335.

MEI, C. C., HARA, T. & NACIRI, M. 1988 Note on Bragg scattering of water waves by parallel bars on the seabed. *J. Fluid Mech.* **186**, 147–162.

https://doi.org/10.1017/jfm.2018.817 Published online by Cambridge University Press

MESSING, R. & KLOKER, M. J. 2010 Investigation of suction for laminar flow control of three-dimensional boundary layers. *J. Fluid Mech.* **658**, 117–147.

NAYFEH, A. H., RAGAB, S. A. & AL-MAAITAH, A. A. 1988 Effect of bulges on the stability of boundary layers. *Phys. Fluids* **31** (4), 796–806.

NG, L. L. & CROUCH, J. D. 1999 Roughness-induced receptivity to crossflow vortices on a swept wing. *Phys. Fluids* **11** (2), 432–438.

PARK, D. & PARK, S. O. 2013 Linear and non-linear stability analysis of incompressible boundary layer over a two-dimensional hump. *Comput. Fluids* **73**, 80–96.

RADEZTSKY, R. H., REIBERT, M. S. & SARIC, W. S. 1999 Effect of isolated micron-sized roughness on transition in swept-wing flows. *AIAA J.* **37** (11), 1370–1377.

REIBERT, M. S., SARIC, W. S., CARRILLO, R. B. JR. & CHAPMAN, K. L. 1996 Experiments in nonlinear saturation of stationary crossflow vortices in a swept-wing boundary layer. *AIAA Paper* 1996-0184.

RIZZETTA, D. P., VISBAL, M. R., REED, H. L. & SARIC, W. S. 2010 Direct numerical simulation of discrete roughness on a swept-wing leading edge. *AIAA J.* **48** (11), 2660–2673.

SARIC, W. S., CARRILLO, R. B. JR. & REIBERT, M. S. 1998 Leading-edge roughness as a transition control mechanism. *AIAA Paper* 1998-0781.

SARIC, W. S. & REED, H. L. 2003 Crossflow instabilities: theory and technology. *AIAA Paper* 2003-771.

SARIC, W. S., REED, H. L. & KERSCHEN, E. J. 2002 Boundary-layer receptivity to freestream disturbances. *Annu. Rev. Fluid Mech.* **34** (1), 291–319.

SARIC, W. S., REED, H. L. & WHITE, E. B. 2003 Stability and transition of three-dimensional boundary layers. *Annu. Rev. Fluid Mech.* **35** (1), 413–440.

SCHRADER, L.-U., BRANDT, L. & HENNINGSON, D. S. 2009 Receptivity mechanisms in three-dimensional boundary-layer flows. *J. Fluid Mech.* **618**, 209–241.

TEMPELMANN, D., SCHRADER, L.-U., HANIFI, A., BRANDT, L. & HENNINGSON, D. S. 2012 Swept wing boundary-layer receptivity to localized surface roughness. *J. Fluid Mech.* **711**, 516–544.

THOMAS, C., MUGHAL, S. & ASHWORTH, R. 2017 Development of Tollmien–Schlichting disturbances in the presence of laminar separation bubbles on an unswept infinite wavy wing. *Phys. Rev. Fluids* **2** (4), 043903.

THOMAS, C., MUGHAL, S., GIPON, M., ASHWORTH, R. & MARTINEZ-CAVA, A. 2016 Stability of an infinite swept wing boundary layer with surface waviness. *AIAA J.* **54** (10), 3024–3038.

WASSERMANN, P. & KLOKER, M. J. 2002 Mechanisms and passive control of crossflow-vortex-induced transition in a three-dimensional boundary layer. *J. Fluid Mech.* **456**, 49–84.

WIE, Y.-S. & MALIK, M. R. 1998 Effect of surface waviness on boundary-layer transition in two-dimensional flow. *Comput. Fluids* **27** (2), 157–181.

WOODRUFF, M. J., SARIC, W. S. & REED, H. L. 2011 Receptivity measurements on a swept-wing model. *AIAA Paper* 2011-3882.

WU, X. & DONG, M. 2016 A local scattering theory for the effects of isolated roughness on boundary-layer instability and transition: transmission coefficient as an eigenvalue. *J. Fluid Mech.* **794**, 68–108.

https://doi.org/10.1017/jfm.2018.817 Published online by Cambridge University Press